Missouri S&T Library and Learning Resources

Scholars' Mine

Masters Theses | Student Theses and Dissertations

Fall 2015

An improved planar cavity model for dielectric characterization

Benjamin Jay Conley

Follow this and additional works at: https://scholarsmine.mst.edu/masters_theses

Part of the Electromagnetics and Photonics Commons

Department:

Recommended Citation

Conley, Benjamin Jay, "An improved planar cavity model for dielectric characterization" (2015). *Masters Theses*. 7462.
https://scholarsmine.mst.edu/masters_theses/7462

This thesis is brought to you by Scholars' Mine, a service of the Missouri S&T Library and Learning Resources. This work is protected by U. S. Copyright Law. Unauthorized use including reproduction for redistribution requires the permission of the copyright holder. For more information, please contact scholarsmine@mst.edu.

AN IMPROVED PLANAR CAVITY MODEL FOR DIELECTRIC

CHARACTERIZATION

by

BENJAMIN JAY CONLEY

A THESIS

Presented to the Faculty of the Graduate School of the

MISSOURI UNIVERSITY OF SCIENCE AND TECHNOLOGY

In Partial Fulfillment of the Requirements for the Degree

MASTER OF SCIENCE IN ELECTRICAL ENGINEERING

2015

Approved by:

Jun Fan, Advisor
Reza Zoughi
Victor Khilkevich

ABSTRACT

Accurate characterization of the dielectric properties of the laminate materials used in printed circuit board fabrication is critical for maximizing the performance of modern high speed circuitry. While many techniques exist for characterizing dielectric materials, most existing techniques are either limited in accuracy or highly impractical for use with planar, copper-clad laminate sheets. A common method involves forming a cavity from the printed circuit board material and calculating the permittivity and dissipation factor from the measured resonant frequencies and quality factor of the cavity. This resonance technique makes the assumption of an ideal cavity, which leads to errors in both measured permittivity and dissipation factor. A more accurate model is proposed that de-embeds the effects of dielectric loss, surface conductivity and reactance, surface roughness, and cavity coupling efficiency. The influence of each of these non-ideal effects on measured dielectric parameters is quantified through mathematical analysis and numerical simulation. Measurements on physical cavities are performed to verify the new model.

ACKNOWLEDGMENTS

I would first like to thank my advisor, Dr. Jun Fan, for his guidance and support throughout my MS program. I would like to thank Dr. Victor Khilkevich for his willingness to be part of my thesis committee. I would also like to thank my undergraduate advisor and committee member Dr. Reza Zoughi, for it is he who convinced me to pursue a graduate degree in the first place.

I am extremely grateful for the undying support and encouragement of my parents and grandparents, without whom none of this would be possible.

TABLE OF CONTENTS

Page

ABSTRACT iii

ACKNOWLEDGMENTS iv

LIST OF ILLUSTRATIONS vii

LIST OF TABLES x

NOMENCLATURE xi

SECTION

1. INTRODUCTION 1
    1.1. DIELECTRIC MATERIALS 1
    1.2. COMMON METHODS FOR DIELECTRIC CHARACTERIZATION OF PLANAR MATERIALS 3
    1.3. STRUCTURE OF THIS THESIS 4
2. IDEAL CAVITY RESONANCE 5
    2.1. GENERAL CONDITIONS OF RESONANCE 5
    2.2. RESONANCE IN RECTANGULAR ELECTROMAGNETIC CAVITIES 7
    2.3. FIELD PATTERNS OF THE TE_{m0l} MODE 12
    2.4. ENERGY STORED IN AN IDEAL PLANAR CAVITY 14
    2.5. USE OF CAVITY RESONANCE MEASUREMENTS TO CHARACTERIZE DIELECTRIC MATERIALS 15
        2.5.1. Calculation of ϵ' and ϵ'' from Measured Resonance Characteristics. 15
        2.5.2. Inaccuracies in the Ideal Cavity Assumption. 16
3. DEVELOPMENT OF AN IMPROVED MODEL 18
    3.1. EFFECT OF DIELECTRIC LOSS ON RESONANT FREQUENCY 18
        3.1.1. Mathematical Derivation. 18
        3.1.2. Analysis. 19
    3.2. EFFECT OF SURFACE CONDUCTIVITY ON Q-FACTOR 20
        3.2.1. Mathematical Derivation. 20
        3.2.2. Analysis. 23
    3.3. EFFECT OF SURFACE CONDUCTIVITY ON FREQUENCY 26

3.3.1. Mathematical Derivation. 26
3.3.2. Analysis. 31
3.4. EFFECT OF CONDUCTOR SURFACE ROUGHNESS ON Q-FACTOR 33
3.4.1. Hammerstad-Jensen Model. 35
3.4.2. Hall Hemispherical Model. 36
3.4.3. Huray Snowball Model. 38
3.4.4. Analysis. 39
3.5. EFFECT OF CAVITY COUPLING ON Q-FACTOR 42
3.5.1. Mathematical Derivation. 42
3.5.2. Analysis. 47
3.6. EFFECT OF COUPLING COEFFICIENT ON FREQUENCY 52
3.6.1. Empirical Method Development. 52
3.6.2. Analysis. 53
3.7. DIELECTRIC CHARACTERIZATION PROCEDURE 54
4. VERIFICATION OF THE IMPROVED MODEL THROUGH NUMERICAL SIMULATION 57
4.1. EFFECT OF DIELECTRIC LOSS ON RESONANT FREQUENCY 57
4.2. EFFECT OF SURFACE CONDUCTIVITY ON Q-FACTOR 58
4.3. EFFECT OF SURFACE CONDUCTIVITY ON FREQUENCY 61
4.4. EFFECT OF CONDUCTOR SURFACE ROUGHNESS ON Q-FACTOR 63
4.5. EFFECT OF CAVITY COUPLING ON Q-FACTOR 67
4.6. SIMULATED DIELECTRIC CHARACTERIZATION 67
5. VERIFICATION OF THE IMPROVED MODEL THROUGH PHYSICAL MEASUREMENT 70
5.1. CAVITY CONSTRUCTION 70
5.2. SURFACE ROUGHNESS MEASUREMENTS 71
5.3. ELECTRICAL MEASUREMENTS 73
5.4. ANALYSIS 75
6. CONCLUSION 78
BIBLIOGRAPHY 79
VITA. 81

LIST OF ILLUSTRATIONS

Page

Figure 2.1. Diagram of a general reflection resonance 7

Figure 2.2. Physical dimensions and mode numbers of a rectangular waveguide cavity 8

Figure 2.3. First 15 resonant frequencies of a 50x40x1 mm cavity 11

Figure 3.1. Resonant frequency change vs. dielectric loss tangent 19

Figure 3.2. Error in measured ϵ' vs. dielectric loss tangent 20

Figure 3.3. Calculated Q_{smooth} of the first 15 resonant modes of an example cavity ... 24

Figure 3.4. Error in measured $\tan(\delta_d)$ caused by neglecting Q_{smooth} in an example cavity 25

Figure 3.5. Relative influence of the side walls and top/bottom walls of an example cavity on the total Q factor at the dominant frequency 26

Figure 3.6. Resonant frequency of a TE_{101} example cavity as a function of σ_c 31

Figure 3.7. Change in resonant frequency of a TE_{101} example cavity as a function of σ_c 32

Figure 3.8. Error in permittivity measurement caused by neglecting finite wall conductivity in a TE_{101} example cavity as a function of σ_c 32

Figure 3.9. Error in permittivity measurement caused by neglecting finite wall conductivity in an example cavity as a function of resonant mode 33

Figure 3.10. Cross sectional image of conductor surface roughness 34

Figure 3.11. Surface profile assumed by the Hammerstad-Jensen model 35

Figure 3.12. Surface profile assumed by the Hall Hemispherical model 36

Figure 3.13. Top view of the surface profile assumed by Hall Hemispherical model 36

Figure 3.14. Surface profile assumed by the Huray Snowball model 38

Figure 3.15. Calculated roughness coefficient 40

Figure 3.16. Comparison of Q-factor for smooth and rough conductors as a function of frequency 41

Figure 3.17. Error in measured dissipation factor due to surface roughness as a function of $\tan(\delta_d)$ for ϵ_r' in a TE_{101} 50x40x1 mm cavity 41

Figure 3.18. Equivalent circuit of a cavity resonator 42

Figure 3.19. Simplified equivalent circuit of a cavity resonator 44

Figure 3.20. Smith chart representation of an overcoupled and undercoupled resonance 45
Figure 3.21. Graphical representation of $\Delta\omega_\rho$ 47
Figure 3.22. Image of the frequency-domain CST SMA-excitation model 48
Figure 3.23. Smith chart representation of simulated $|S_{11}|$ results of a TE_{101} mode 50x40x1 mm cavity filled with Rogers 4350 48
Figure 3.24. Simulated $|S_{11}|$ results of a TE_{101} mode 50x40x1 mm cavity filled with Rogers 4350 49
Figure 3.25. Calculated external, internal, and loaded Q-factors as a function of $\mathscr{k}$ for simulated data 50
Figure 3.26. Difference between Q_{int} and Q_L as a function of $\mathscr{k}$ 51
Figure 3.27. Error in calculated $\tan(\delta_d)$ caused by neglecting Q_{ext} as a function of $\mathscr{k}$. 51
Figure 3.28. Shift in resonant frequency of a TE_{101} 50x40x1 mm cavity as a function of coupling coefficient 53
Figure 3.29. Error in calculated ϵ' in a TE_{101} 50x40x1 mm cavity as a function of coupling coefficient 54
Figure 4.1. Comparison between the analytical solution and HFSS eigenmode solution of the change in resonant frequency due to dielectric loss 57
Figure 4.2. Difference between the analytical solution and HFSS eigenmode solution of the change in resonant frequency due to dielectric loss 58
Figure 4.3. Comparison between the analytical solution and HFSS eigenmode solution of Q_{smooth} as a function of cavity wall conductivity 59
Figure 4.4. Difference between the analytical and HFSS eigenmode solutions of Q_{smooth} as a function of surface conductivity 60
Figure 4.5. Difference between the analytical and HFSS eigenmode solutions of Q_{smooth} as a function of resonant mode for an example cavity 60
Figure 4.6. Comparison between the analytical and HFSS eigenmode solutions of f_r as a function of σ_c for an example cavity 61
Figure 4.7. Difference between the analytical and HFSS eigenmode solutions of f_r as a function of σ_c for an example cavity 62
Figure 4.8. Difference between the analytical and HFSS eigenmode solutions of f_r as a function of resonant mode for an example cavity 62
Figure 4.9. Simulated stripline structure used to model the effects of conductor surface roughness 63
Figure 4.10. Close-up image of the rough stripline model used in simulation 64
Figure 4.11. Calculated roughness factor for simulated stripline surface 65

Figure 4.12. Comparison of simulated $|S_{21}|$ results of a rough stripline and the Hall Hemispherical model 66

Figure 4.13. Difference between analytical and HFSS eigenmode solutions of Q_{int} as a function of k 67

Figure 4.14. Simulated $|S_{11}|$ used to test dielectric characterization procedure 68

Figure 5.1. 55x50x1.6 mm cavity made with Rogers 5880 laminate 70

Figure 5.2. Milling process for removing SMA GND pins 71

Figure 5.3. SEM image of PCB laminate cross section 72

Figure 5.4. SEM image of conductor surface roughness 72

Figure 5.5. Calculated roughness coefficient vs. frequency for physical cavity 73

Figure 5.6. Measured reflection response of 55.3x50.0x1.57 mm cavity 74

Figure 5.7. Smith chart representation of measured reflection response 74

LIST OF TABLES

Page

Table 4.1. Simulated surface roughness parameters 66
Table 4.2. Simulated dielectric characterization results 69
Table 5.1. Measured roughness parameters 73
Table 5.2. Measured dielectric properties for 58.3x49.8 mm cavity 75
Table 5.3. Measured dielectric properties for 55.3x50 mm cavity 75

NOMENCLATURE

Symbol	Description
E	Electric field vector
D	Electric flux density vector
H	Magnetic field vector
B	Magnetic flux density vector
ϵ	Complex permittivity
μ	Complex permeability
ϵ_r	Relative permittivity
ϵ_d, μ_d	Permittivity and permeability of dielectric material
$\tan(\delta_d)$	Electric dissipation factor
ϵ_0	Permittivity of free space
μ_0	Permeability of free space
c	Speed of light in free space
σ_d	Effective dielectric conductivity in $\left(\frac{\mathrm{S}}{\mathrm{m}}\right)$
σ_s	Static field dielectric conductivity
σ_a	Alternating field dielectric conductivity
σ_c	Conductivity of electrical conductor
ω	Angular velocity in $\left(\frac{\mathrm{rad}}{\mathrm{sec}}\right)$
v_p	Phase velocity
Γ	Complex voltage reflection coefficient
λ	Wavelength through dielectric material
f_r, ω_r	Resonant frequency and angular velocity
f_{ideal}	Ideal resonant frequency
f_L	Resonant frequency loaded by external circuit
f_u	Unloaded resonant frequency
a, b, d	Cavity dimensions in (m) along X, Y, and Z axes
m, n, ℓ	Mode numbers along X, Y, and Z axes
γ	Complex propagation constant
α	Attenuation constant in spatial domain
β_0	Wave number in unbounded medium
$\beta_x, \beta_y, \beta_z$	Directional bounded medium wave numbers

β_c	Cutoff wave number in waveguide
W_e, W_m	Energy stored in electric and magnetic fields
Q_{meas}	Measured Q-factor
Q_d	Q-factor due to dielectric loss
Q_{smooth}	Q-factor due to smooth conductor resistivity
Q_{rough}	Q-factor due to surface roughness losses
Q_c	Q-factor due to conductor loss
Q_{int}	Q-factor due to internal losses
Q_{ext}	Q-factor due to external coupling network
Q_L	Loaded Q-factor
Q_{rad}	Q-factor due to radiation loss
Q_{TB}	Q-factor due to resistivity in the top and bottom walls
Q_{sides}	Q-factor due to resistivity in the side walls
R_s	Surface resistivity
P_{smooth}	Power lost in the smooth conductive walls
P_{TB}	Power lost in the top and bottom walls
P_{sides}	Power lost in the side walls
ξ	Roughness loss coefficient
δ	Skin depth
h_{RMS}	RMS roughness height in m
B_{RMS}	RMS roughness base width in m
s_{RMS}	RMS roughness spacing in m
$\mathscr{k}$	Cavity coupling coefficient
ρ	Voltage reflection coefficient magnitude

1. INTRODUCTION

1.1. DIELECTRIC MATERIALS

Material characteristics play an important role in the design of high frequency electronic circuits and structures. The dielectric material through which an electromagnetic wave propagates affects the velocity, wavelength, and attenuation of the wave, as well as characteristic impedance in a transmission line. It is of utmost importance, then, for high speed printed circuit board (PCB) designers to accurately know the dielectric properties of the materials that compose their designs.

The electric flux density **D** is related to the electric field **E** by [1]

$$\mathbf{D} = \epsilon \mathbf{E} \tag{1}$$

where ϵ is called the permittivity and is, simply put, a representation of a material's ability to concentrate an electric field. The magnetic flux density **B** is likewise related to the magnetic field **H** by the material's permeability μ:

$$\mathbf{B} = \mu \mathbf{H} \tag{2}$$

The parameters ϵ and μ are complex quantities given by

$$\epsilon = \epsilon' - j\epsilon'' \tag{3}$$

$$\mu = \mu' - j\mu'' \tag{4}$$

The real parts of ϵ and μ relate to the material's ability to concentrate electric and magnetic fields, respectively. The imaginary components represent frequency dependent loss due to electric or magnetic conductivity in the material.

In free space, the permittivity and permeability take the values of $\epsilon_0 = 8.854 \times 10^{-12} \frac{\mathrm{As}}{\mathrm{Vm}}$ and $\mu_0 = 4\pi \times 10^{-7} \frac{\mathrm{Vs}}{\mathrm{Am}}$. The speed of light in a vacuum c is dependent upon the values of ϵ_0 and μ_0

$$c = \sqrt{\frac{1}{\mu_0 \epsilon_0}} \tag{5}$$

It is common when referring to dielectric materials to normalize the values of ϵ and μ against their respective free space values, such that

$$\epsilon_r = \frac{\epsilon'}{\epsilon_0} \tag{6}$$

$$\mu_r = \frac{\mu'}{\mu_0} \tag{7}$$

where the subscript "r" means "relative". In the materials typically used in PCB fabrication, $\mu = \mu_0$. Thus, to model the behavior of a PCB dielectric material, it is only necessary to characterize the permittivity. Relative permeability is almost always assumed to be 1.

Dielectric loss is caused by a combination of static electrical conductivity σ_s and alternating field dipole hysteresis $\sigma_a = \omega\epsilon''$ [2]. The effective dielectric conductivity σ_d is the sum of σ_s and σ_a

$$\sigma_d = \sigma_s + \sigma_a \tag{8}$$

A common term for describing dielectric loss is the dissipation factor $\tan(\delta_d)$, which is expressed by

$$\tan(\delta_d) = \frac{\sigma_d}{\omega\epsilon'} \tag{9}$$

In most dielectric materials, $\sigma_s \ll \omega\epsilon''$. The dissipation factor can then be written as

$$\tan(\delta_d) = \frac{\sigma_s + \omega\epsilon''}{\omega\epsilon'} \cong \frac{\epsilon''}{\epsilon'} \tag{10}$$

1.2. COMMON METHODS FOR DIELECTRIC CHARACTERIZATION OF PLANAR MATERIALS

A good overview of techniques for dielectric characterization is given in [3], though many of the techniques listed are not suitable for use on PCB substrates because of the presence of conductive layers on the material. A few specialized techniques take advantage of the conductive layers and use them as part of the testing procedure. The simplest of these techniques treats the PCB panel as a parallel plate capacitor. Given a known plate surface area and dielectric thickness, the capacitance of the panel can be measured using an LCR meter or impedance analyzer. Material ϵ' can then be calculated from the measured capacitance and $\tan(\delta_d)$ from the capacitor's dissipation. The capacitance technique is limited in accuracy by the fringing fields near the plates' edges. Additionally, this technique only works at lower frequencies where the capacitive structure is electrically small. At higher frequencies, the lumped element capacitor assumption is no longer valid.

Another technique involves measuring the phase and attenuation constants along a planar transmission (e.g. microstrip or stripline). In this method, vector transmission measurements are made using a vector network analyzer (VNA) to extract the necessary transmission line parameters. To avoid the influence of return loss, it is necessary to perform de-embedding of the connector-to-line transition. This travelling wave technique provides information on the *effective* dielectric constant, which is influenced by surrounding media, dielectric anisotropy, and conductor geometry and surface roughness. In some instances, knowledge of the effective dielectric constant for a particular line geometry is preferred to that of the physical dielectric constant (i.e., the dielectric constant of the material itself). If an accurate characterization of the physical dielectric constant is needed, then the travelling wave technique is not ideal.

If a PCB panel is used as a cavity resonator, then ϵ' can be determined from the resonant frequency and $\tan(\delta_d)$ from the resonant quality factor. The IPC-TM-650 standard [4] outlines such a technique, which IPC calls the "full sheet resonance" (FSR) method. In this test standard, two conductive planes of a dielectric panel are driven against each other to excite the cavity formed between the conductors. The top and bottom planes are not connected to each other along the edges of the sheet, resulting in a

substantial amount of radiation loss. Non-ideal effects such as surface roughness and finite conductivity are also neglected. The IPC standard does not recommend this method for use in absolute measurements of ϵ' or $\tan(\delta_d)$, both of which will be rendered inaccurate because of the assumptions made. This technique does, however, provide a simple way to compare the properties of two or more dielectric sheets. If an accurate characterization on a single panel has been performed using another method, then the FSR results of this "calibrated" panel can be compared to results from other panels to identify deviations in dielectric properties across a production batch.

If the non-ideal effects neglected by the FSR technique can be calculated and mathematically removed in post-processing, then it should be possible to characterize the absolute dielectric properties of a material using a sheet resonance method. Such analysis is the purpose of this thesis.

1.3. STRUCTURE OF THIS THESIS

Section 2 presents the basic conditions of resonance for electromagnetic resonators and discusses the behavior of ideal rectangular waveguide cavities. A simplified methodology is presented to calculate ϵ' and $\tan(\delta_d)$. Section 3 provides mathematical analysis for each aspect of a cavity's non-ideal behavior. The effects of each assumption on dielectric measurement accuracy are explored using a hypothetical example cavity. A step-by-step guide to using the techniques presented herein is included at the end of Section 3. Section 4 presents full wave numerical simulation results and compares the results to those calculated analytically in Section 3. Measurements of a physical cavity are made in Section 5, as are final comments on the accuracy of the proposed methodology.

2. IDEAL CAVITY RESONANCE

2.1. GENERAL CONDITIONS OF RESONANCE

An electromagnetic resonator can be thought of as a section of a wave guiding structure with each end terminated in a non-matched impedance. The wave guiding structure can be of any type, including coaxial cable, microstrip lines, and hollow waveguides. Because of the applications of the work in this thesis to planar materials, however, only rectangular waveguide cavities are analyzed herein, as rectangular geometries are the simplest to fabricate out of PCB material. Nevertheless, the following discussion of ideal resonance conditions applies to all guided wave resonators.

If an electromagnetic wave is coupled into the wave transmission section of a resonator, it will propagate until reaching an impedance discontinuity located at the resonator ends. This discontinuity can be in the form of an open-circuit (resulting in reflection coefficient, Γ, of $+1$ or $1\angle 0°$) or a short circuit ($\Gamma = -1$ or $1\angle -180°$).

After being reflected off the discontinuity at one end of the resonator, the travelling wave will then propagate in the other direction until being reflected by the discontinuity at the other end of the line. Thus, the wave will be continually reflected in alternating directions along the structure. If the travelling wave is in phase with the excitation wave after a round-trip through the line, the condition for resonance is satisfied. This phase matching occurs when the phase shift along the line is an integer multiple of 2π radians. In other words, the electrical round-trip length of the line must be an integer multiple of the wavelength of the travelling wave for resonance to occur. Mathematically, this is represented by:

$$\frac{2\pi}{\lambda}(2L_{line}) + \angle(\Gamma_1) + \angle(\Gamma_2) = 2\pi k \tag{11}$$

where λ is the wavelength of the travelling wave in the guided wave structure, $\angle(\Gamma_1)$ and $\angle(\Gamma_2)$ are the phases of reflection coefficients at each end of the line, L_{line} is the length of the line, and k is an integer representing the number of wavelengths present in the round-trip length of the structure. The presence of k in (9) indicates that multiple

resonant frequencies are supported by a single resonator geometry. Each of these multiple resonances is called a resonant "mode". Modes are identified based on the number of half-wavelengths established along the resonator. In an ideal resonator, an infinite number of modes can be supported, though the characteristics of physical materials provide a limit on the highest frequencies achievable. It is worth noting that (11) can be satisfied when both $\angle(\Gamma_1)$ and $\angle(\Gamma_2)$ are either 0° or $180°$. This leads to the conclusion that, at least in ideal resonators, the reflectors can be either both open or short circuits with no change in resonant frequency.

The in-phase reflected travelling waves will add constructively to form a standing wave along the length of the resonator. Waves at frequencies other than those of the resonant modes will undergo destructive interference and decay in amplitude. The rate of decay depends upon the difference in frequency from the resonant standing wave. In a resonator that contains no losses, all waves at frequencies other than the resonant modes will remain at the amplitude of excitation, while the resonant frequencies will add constructively to a theoretical infinite amplitude. In a lossy resonator, waves at the resonant frequencies will also decay to some extent. This decay is expressed in terms of quality factor (also called Q-factor or simply "Q"). The Q is a unitless quantity defined as the ratio between power stored by the resonator and power lost to heat and other mechanisms.

$$Q = \frac{P_{stored}}{P_{lost}} \tag{12}$$

A sample resonance is shown in Figure 2.1. This figure shows the simulated $|S_{11}|$ response of a rectangular cavity excited with a swept-frequency source. The resonant frequency f_r is found at the center of the null occurring at 1.882 GHz. The null in $|S_{11}|$ indicates that power is being stored in the resonator at this frequency. As frequency moves away from f_r, $|S_{11}|$ begins to increase until nearly all the input power is reflected at the edges of the displayed frequency span. In the figure, Δf represents the width of the resonance at an arbitrary value of $|S_{11}|$. The method for calculating Q from f_r and Δf is presented in Section 3.5.

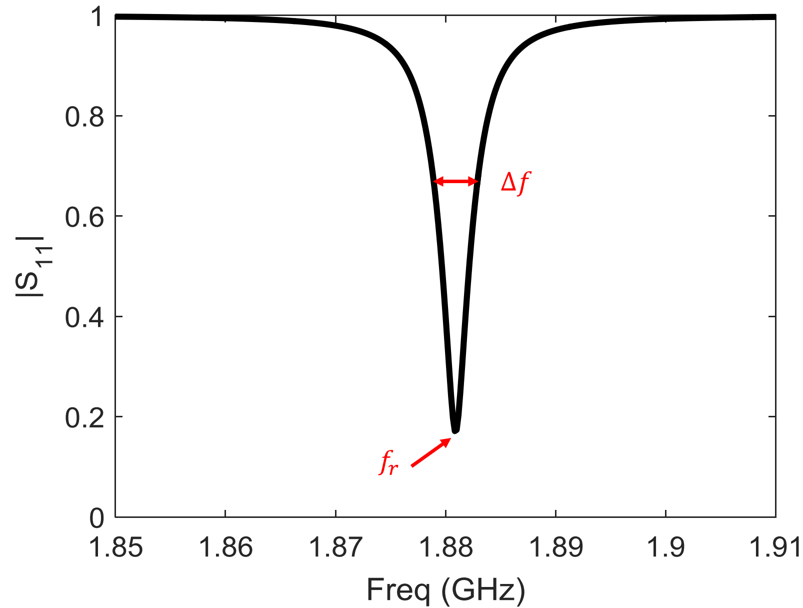

Figure 2.1. Diagram of a general reflection resonance. $f_r = 1.882$ GHz and $\Delta f = 7.3$ MHz.

2.2. RESONANCE IN RECTANGULAR ELECTROMAGNETIC CAVITIES

While the principles outlined in Section 2.1 are applicable to all electromagnetic resonators, individual resonator types must be analyzed separately to account for their unique geometries and boundary conditions. The mathematical formulation of resonance behavior for ideal rectangular waveguide cavities is presented in this section. An ideal cavity is filled with a lossless dielectric material and has perfectly conducting walls. As will be seen in later sections, these assumptions of ideality lead to errors in modelling the resonance.

The discussion in Section 2.1 pertained to a wave guiding structure in which wave propagation was limited to a single direction. In the case of a generalized rectangular cavity resonator, standing waves can be established along each of the three Cartesian axes. The number of $\frac{\lambda}{2}$ standing waves along the a, b, d dimensions of the cavity are denoted by positive integers m, n, and ℓ along the X, Y, and Z axes, respectively, as shown in Figure 2.2. In this notation, $b \leq a \leq d$.

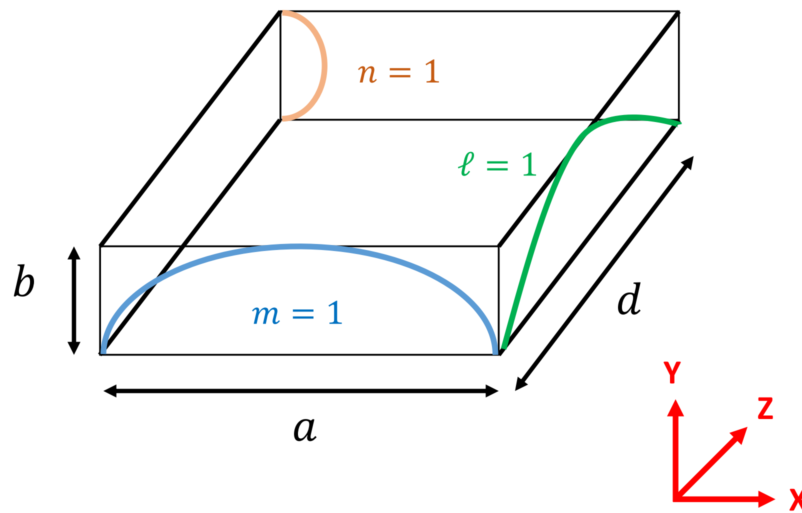

Figure 2.2. Physical dimensions and mode numbers of a rectangular waveguide cavity

In unbounded media, electromagnetic waves propagate in the transverse-electromagnetic (TEM) form, where both the electric and magnetic field components of the wave are orthogonal to each other and the direction of wave propagation. In rectangular waveguides and cavities, waves can propagate as either transverse-electric (TE) or transverse-magnetic (TM) waves, where either (but not both) the electric field or magnetic are orthogonal to the direction of propagation. TE modes are constrained such that $m = 0, 1, 2, \ldots$, $n = 0, 1, 2, \ldots$, and $\ell = 1, 2, 3, \ldots$ Either m or n can be equal to zero, but not both. In TM modes, $m = 1, 2, 3, \ldots$, $n = 1, 2, 3, \ldots$, and $\ell = 0, 1, 2, \ldots$ Because of the planar cavity condition that $b \ll a$ and the resulting fact that $n = 0$ for the first several resonant modes, the planar cavity is restricted to operation in the TE modes. The electric field $\boldsymbol{E}$ at position z travelling through a dielectric medium can be written as [2]

$$\boldsymbol{E}(z) = \hat{\boldsymbol{a}}_x E_x(z) = \hat{\boldsymbol{a}}_x (E_0^+ e^{-\gamma z} + E_0^- e^{+\gamma z}) \tag{13}$$

In (13), γ is known as the complex propagation constant which describes how the phase and amplitude of a wave change with respect to position z and is given by

$$\gamma = \alpha + j\beta_0 = \sqrt{j\omega\mu_d(\sigma_d + j\omega\epsilon_d')} = \sqrt{-\omega^2\mu_d\epsilon_d' + j\omega\mu_d\sigma_d} \qquad (14)$$

where μ_d is the permeability of the medium, ϵ_d is the permittivity of the medium, σ_d is the conductivity of the medium, and ω is the angular velocity of the wave. The real valued term α is the attenuation constant in $\frac{Np}{m}$ and β_0 is the phase constant (also called wave number) in $\frac{Rad}{m}$. The phase constant can also be defined as

$$\beta_0 = \frac{\lambda_0}{2\pi} \qquad (15)$$

where λ_0 is the wavelength in the unbounded dielectric medium. If a lossless medium is assumed, then $\sigma_d = 0$ and

$$\beta_0 = \omega\sqrt{\mu_d\epsilon_d'} \qquad (16)$$

In a bounded medium such as a rectangular cavity, β_0 is further constrained by dispersion equation:

$$\beta_0^2 = \beta_x^2 + \beta_y^2 + \beta_z^2 \qquad (17)$$

The β_x, β_y, and β_z terms in (17) are called the directional wave numbers and are given by

$$\beta_x = \frac{2\pi}{\lambda_x} \qquad (18)$$

$$\beta_y = \frac{2\pi}{\lambda_y} \tag{19}$$

$$\beta_z = \frac{2\pi}{\lambda_z} \tag{20}$$

Combining (16) through (20) yields

$$\omega_r\sqrt{\mu_d\epsilon_d'} = \sqrt{\left(\frac{2\pi}{\lambda_x}\right)^2 + \left(\frac{2\pi}{\lambda_y}\right)^2 + \left(\frac{2\pi}{\lambda_z}\right)^2} \tag{21}$$

Given the assumption of an ideal cavity and perfectly reflecting walls, (11) becomes

$$\frac{2\pi}{\lambda}(2L_{line}) = 2\pi k \tag{22}$$

Solving for λ,

$$\lambda = \frac{2L_{line}}{k} \tag{23}$$

In this equation, λ should be replaced by λ_x, λ_y, or λ_z, L_{line} by a, b, or d, and k by m, n, or ℓ for each of the three Cartesian axes, respectively. Substituting (23) into (21) gives

$$\omega_r\sqrt{\mu_d\epsilon_d'} = \sqrt{\left(\frac{m\pi}{a}\right)^2 + \left(\frac{n\pi}{b}\right)^2 + \left(\frac{\ell\pi}{d}\right)^2} \tag{24}$$

Solving (24) for frequency produces the formula for the resonant frequency of an ideal cavity:

$$f_{ideal} = \frac{1}{2\pi\sqrt{\mu_d \epsilon_d'}} \sqrt{\left(\frac{m\pi}{a}\right)^2 + \left(\frac{n\pi}{b}\right)^2 + \left(\frac{\ell\pi}{d}\right)^2} \tag{25}$$

Additionally, the directional wave numbers can be written as

$$\beta_x = \frac{m\pi}{a} \tag{26}$$

$$\beta_y = \frac{n\pi}{b} \tag{27}$$

$$\beta_z = \frac{\ell\pi}{d} \tag{28}$$

The lowest resonant frequency will occur when $m = 1$, n= 0, and $\ell = 1$ in a planar cavity, while higher order modes will resonate at higher frequencies. Depending on the cavity geometry, it is possible for multiple modes to have nearly the same resonant frequencies, as shown in Figure 2.3. Modal overlap is said to occur if two frequencies are close enough together such that they are difficult to distinguish from each other. In Figure 2.3, modes 6 and 7 are likely to exhibit modal overlap because of their proximity in frequency.

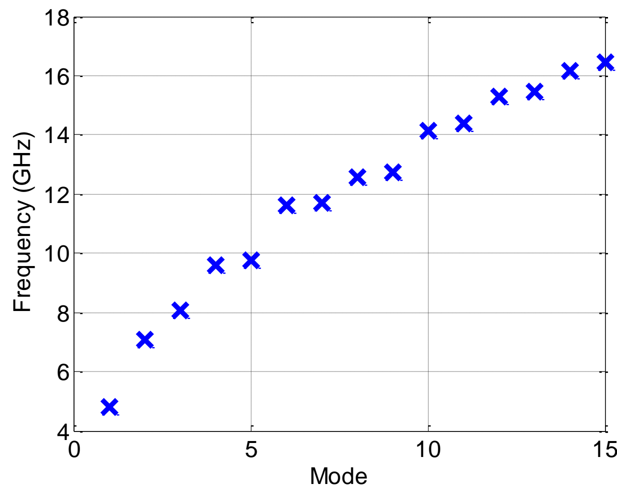

Figure 2.3. First 15 resonant frequencies of a 50x40x1 mm cavity

2.3. FIELD PATTERNS OF THE TE$_{m0\ell}$ MODE

When analyzing rectangular cavities, it becomes useful to have mathematical expressions for the standing waves present inside the resonating structure. While a derivation directly from Maxwell's equations is possible, this approach proves to be very time consuming. An easier method is to begin with the field patterns of a rectangular wave operating in the TE$_{\mathrm{mn}}$ mode. The expressions for $\boldsymbol{E}$ and $\boldsymbol{H}$ are given in (29) and (30), respectively [2].

$$\begin{cases} E_x^+ = \dfrac{A_{mn}\beta_y}{\epsilon_d'}\cos(\beta_x x)\sin(\beta_y y)\, e^{-j\gamma z} \\ E_y^+ = \dfrac{A_{mn}\beta_x}{\epsilon_d'}\sin(\beta_x x)\cos(\beta_y y)\, e^{-j\gamma z} \\ 0 \end{cases} \tag{29}$$

$$\begin{cases} H_x^+ = \dfrac{A_{mn}\beta_x\beta_z}{\omega\epsilon_d'\mu_d}\sin(\beta_x x)\cos(\beta_y y)\, e^{-j\gamma z} \\ H_y^+ = \dfrac{A_{mn}\beta_y\beta_z}{\omega\epsilon_d'\mu_d}\cos(\beta_x x)\sin(\beta_y y)\, e^{-j\gamma z} \\ H_z^+ = -j\dfrac{A_{mn}\left(\beta_x^2 + \beta_y^2\right)}{\omega\epsilon_d'\mu_d}\cos(\beta_x x)\cos(\beta_y y)\, e^{-j\gamma z} \end{cases} \tag{30}$$

where A_{mn} is an amplitude constant. The $e^{-j\gamma z}$ dependence of each field represents the travelling nature of the wave as it propagates through the waveguide.

In a rectangular cavity, waves do not propagate freely along the z-axis; rather, the boundary conditions present at the cavity end walls cause reflections that result in standing wave patterns. These z-axis standing waves cause the expression for E_x in (29) to be written as

$$E_x(x, y, z) = \frac{A_{mn}\beta_y}{\epsilon_d'}\cos(\beta_x x)\sin(\beta_y y)\,[C\cos(\beta_z z) + D\sin(\beta_z z)] \tag{31}$$

where C and D are constants. In a cavity with perfectly conductive end walls, the electric field component tangential to the conductor must be zero. Mathematically, this is given by

$$E_x(0 \le x \le a, 0 \le y \le b, z = 0) = 0 \quad (32)$$

$$E_x(0 \le x \le a, 0 \le y \le b, z = d) = 0 \quad (33)$$

$$E_y(0 \le x \le a, 0 \le y \le b, z = 0) = 0 \quad (34)$$

$$E_y(0 \le x \le a, 0 \le y \le b, z = d) = 0 \quad (35)$$

Applying the boundary condition of (32) to (31) results in

$$\frac{A_{mn}\beta_y}{\epsilon_d'}\cos(\beta_x x)\sin(\beta_y y)\,[C\ (1) + D\ (0)] = 0 \quad (36)$$

Thus, $C = 0$. Likewise, applying (33) to (31) results in

$$\frac{A_{mn}\beta_y}{\epsilon_d'}\cos(\beta_x x)\sin(\beta_y y)\,[D\sin(\beta_z z)] = 0 \quad (37)$$

Because $\beta_z = \frac{\ell\pi}{d}$ as given by (28), $D = 1$. The same values of C and D also apply to E_y. This results in

$$\begin{cases} E_x = \dfrac{\beta_y}{\epsilon_d'} A_{mn\ell}\cos(\beta_x x)\sin(\beta_y y)\sin(\beta_z z) \\ E_y = -\dfrac{\beta_x}{\epsilon_d'} A_{mn\ell}\sin(\beta_x x)\cos(\beta_y y)\sin(\beta_z z) \\ E_z = 0 \end{cases} \quad (38)$$

A similar approach is used to calculate H_z. The PEC boundary condition requires that normal components of the magnetic field be zero. Thus,

$$H_z(0 \le x \le a, 0 \le y \le b, z = 0) = 0 \quad (39)$$

$$H_z(0 \le x \le a, 0 \le y \le b, z = \ell) = 0 \tag{40}$$

Calculating H_z in this manner and enforcing Faraday's Law to calculate H_x and H_y from E_x and E_y results in

$$\begin{cases} H_x = \dfrac{j\beta_x\beta_z A_{mn\ell}}{\omega\mu_d\epsilon_d'}\sin(\beta_x x)\cos(\beta_y y)\cos(\beta_z z) \\ H_y = \dfrac{j\beta_y\beta_z A_{mn\ell}}{\omega\mu_d\epsilon_d'}\cos(\beta_x x)\sin(\beta_y y)\cos(\beta_z z) \\ H_z = -\mathrm{j}\dfrac{A_{mn\ell}}{\omega\mu_d\epsilon_d'}(\beta_x^2 + \beta_y^2)\cos(\beta_x x)\cos(\beta_y y)\sin(\beta_z z) \end{cases} \tag{41}$$

2.4. ENERGY STORED IN AN IDEAL PLANAR CAVITY

The energy stored in the internal electric field of a cavity is given by [5]

$$W_e = \frac{1}{4}\left\{\mathrm{Re}\int_V \mathbf{E}\cdot\mathbf{D}^* dV\right\} \tag{42}$$

Applying (1) results in

$$W_e = \frac{\epsilon_d'}{4}\int_V |\mathbf{E}|^2 dV \tag{43}$$

In a planar cavity, $\beta_y = 0$, and the $\mathrm{TE}_{m0\ell}$ modes dominate. Thus, E_y remains as the only non-zero electric field component. Substituting (38) into (43),

$$W_e = \frac{\epsilon_d'}{4}\left(\frac{m\pi}{a\epsilon_d'}A_{m0\ell}\right)^2 \int_0^d\int_0^b\int_0^a \sin^2\left(\frac{m\pi}{a}x\right)\sin^2\left(\frac{\ell\pi}{d}z\right)dx\,dy\,dz \tag{44}$$

which reduces to

$$W_{\mathrm{e}} = \frac{A_{m0\ell}^2}{\epsilon_d'}\left(\frac{m\pi}{a}\right)^2 \frac{abd}{16} \tag{45}$$

At resonance, the energy stored in the electric field is equal to the energy stored in the magnetic field. Thus,

$$W_{total} = 2W_e = \frac{A_{m0\ell}^2}{\epsilon_d'}\left(\frac{m\pi}{a}\right)^2 \frac{abd}{8} \tag{46}$$

2.5. USE OF CAVITY RESONANCE MEASUREMENTS TO CHARACTERIZE DIELECTRIC MATERIALS

As discussed in Section 1.2, the resonance of an electromagnetic cavity can be used to determine both ϵ_d' and $\tan(\delta_d)$ of a dielectric substrate. The mathematical techniques for determining both parameters from an ideal cavity are presented in this section, followed by a discussion of the problems caused by the assumption of ideality.

2.5.1. Calculation of ϵ' and ϵ'' from Measured Resonance Characteristics. If the resonant frequency of a cavity is known through measurement, (25) can be used to solve for $\sqrt{\mu_d'\epsilon_d'}$. Most dielectric materials used in PCB fabrication can be assumed to have μ values of μ_0, and this assumption allows direct calculation of ϵ_d from the measured resonant frequency and cavity dimensions.

ϵ_d'' and $\tan(\delta_d)$ are representations of dielectric power loss and can be related to Q_d. The power lost in the dielectric material is given by [5]

$$P_d = \frac{\omega\epsilon''}{2}\int_V |\mathbf{E}|^2\, dV \tag{47}$$

which, for a planar cavity, can be written as

$$P_d = \frac{\omega\epsilon''}{2}\left(\frac{m\pi}{a\epsilon_d'}A_{m0\ell}\right)^2 \int_0^d\int_0^b\int_0^a \sin^2\left(\frac{m\pi}{a}x\right)\sin^2\left(\frac{\ell\pi}{d}z\right)dx\,dy\,dz \tag{48}$$

which reduces to

$$P_d = \omega\epsilon'' A_{m0\ell}^2 \left(\frac{m\pi}{a\epsilon_d'}\right)^2 \frac{abd}{8} \tag{49}$$

The Q-factor of the dielectric material is expressed by

$$Q_d = \frac{P_{stored}}{P_d} = \frac{\omega W_{total}}{P_d} = \frac{\epsilon'}{\epsilon''} = \frac{1}{\tan(\delta_d)} \tag{50}$$

Thus, in a perfectly conducting cavity where the dielectric is the only contributor to loss, the dissipation factor can be found by

$$\tan(\delta_d) = \frac{1}{Q_d} \tag{51}$$

2.5.2. Inaccuracies in the Ideal Cavity Assumption. The resonant frequency described in (25) only applies to cavities with lossless dielectrics and smooth, lossless conductors. In reality, the resonant frequency is altered by reactive external coupling networks and internal loss. Likewise, the measured Q of a cavity is influenced by all sources of loss in the cavity and is given by

$$\frac{1}{\mathrm{Q_{meas}}} = \frac{1}{Q_d} + \frac{1}{Q_{smooth}} + \frac{1}{Q_{rough}} + \frac{1}{Q_{ext}} + \frac{1}{Q_{rad}} \tag{52}$$

where Q_{meas} is the measured value, Q_d is caused by dielectric loss, Q_{smooth} is caused by smooth conductor loss, Q_{rough} is caused by internal scattering off the surface roughness of the conductive walls, Q_{ext} is caused by loss in coupling an external signal to the cavity's resonant modes, and Q_{rad} is caused by power lost through radiation. Because the dissipation factor of a dielectric material is given by the reciprocal of Q_d, it is necessary to calculate all other Q factors to be able to solve for Q_d when given Q_{meas}.

Q_{rad} is assumed to be negligible because a conductive cavity is fully enclosed; all other Q factors are to be considered. As such, this thesis addresses and provides mathematical compensation for the following non-idealities:

- The effect of dielectric loss on resonant frequency
- The effect of surface inductance on resonant frequency
- The effect of surface conductivity on Q
- The effect of conductor surface roughness on Q
- The effect of cavity coupling on measured Q
- The effect of cavity coupling on resonant frequency

3. DEVELOPMENT OF AN IMPROVED MODEL

3.1. EFFECT OF DIELECTRIC LOSS ON RESONANT FREQUENCY

In the development of (14) to (16), it was assumed that the dielectric conductivity σ_d is 0. This assumption causes a small error that appears in the final resonance frequency equation. To remove this error, the lossless assumption must not be made.

3.1.1. Mathematical Derivation. Squaring both sides of (14) gives

$$\alpha^2 + 2j\alpha\beta_0 - \beta_0^2 = -\omega^2\mu_d\epsilon_d' + j\omega\mu_d\sigma_d \tag{53}$$

Equating the real and imaginary parts of both sides results in

$$\alpha^2 - \beta_0^2 = -\omega^2\mu_d\epsilon_d' \tag{54}$$

and

$$2\alpha\beta_0 = \omega\mu_d\sigma_d \tag{55}$$

Solving (54) and (55) simultaneously for β_0 results in [2]

$$\beta_0 = \omega\sqrt{\mu_d\epsilon_d'}\sqrt{\frac{1}{2}\left(\sqrt{1 + \left(\frac{\sigma_d}{\omega\epsilon'}\right)^2} + 1\right)} \tag{56}$$

The combination of (9), (17), and (56) yields an expression for resonant frequency that has been compensated for dielectric loss:

$$f_r = \frac{\sqrt{\left(\frac{m\pi}{a}\right)^2 + \left(\frac{n\pi}{b}\right)^2 + \left(\frac{\ell\pi}{d}\right)^2}}{2\pi\sqrt{\mu_d\epsilon_d'}\sqrt{\frac{1}{2}\left(\sqrt{1 + \tan^2(\delta_d)} + 1\right)}} \tag{57}$$

3.1.2. Analysis. Inspection of (57) reveals that the effect of $\tan(\delta_d)$ on f_r is not influenced by cavity geometry or mode of operation. The relative change in f_r can therefore be plotted against $\tan(\delta_d)$ with no loss of generality, as is done in Figure 3.1. The resulting error in ϵ' calculation is shown in Figure 3.2.

Dielectric materials used for PCB substrates are typically chosen to have low values of loss. FR-4, which is arguably the most common low-cost PCB substrate material, has a dissipation factor of 0.016 (though this varies between manufacturers). Rogers 4350, which is a common high performance dielectric material, has a dissipation factor of 0.004 [6]. According to the curve in Figure 3.2, the dielectric loss of both FR-4 and Rogers 4350 will cause an error in measured ϵ' of less than 0.01%. This error is too small to even be measurable in a practical system. As such, the resonant frequency shift due to dielectric loss can be considered negligible.

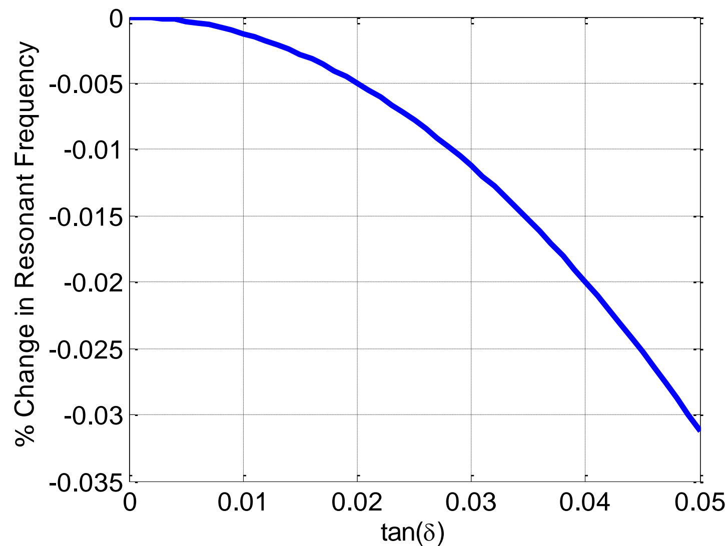

Figure 3.1. Resonant frequency change vs. dielectric loss tangent

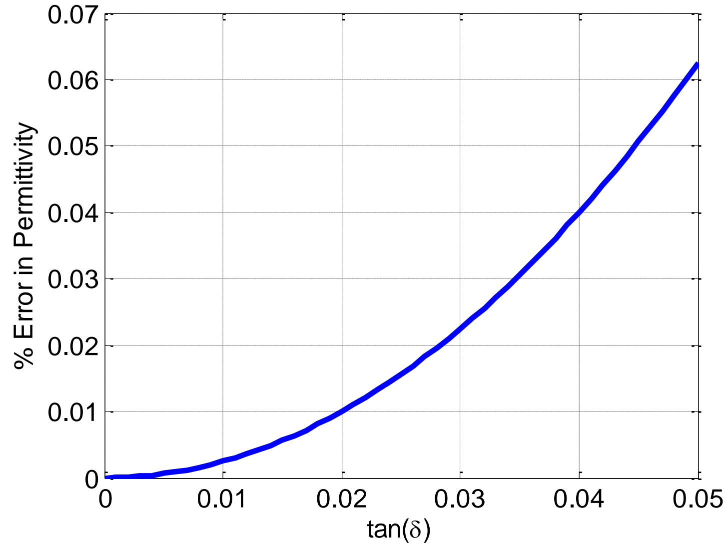

Figure 3.2. Error in measured ϵ' vs. dielectric loss tangent

3.2. EFFECT OF SURFACE CONDUCTIVITY ON Q-FACTOR

To accurately determine the dielectric loss of a material, it is necessary to first calculate the power lost in the conductive walls of the cavity. To do this, it is assumed that the cavity walls are perfectly smooth conductors with an associated quality factor Q_{smooth}. The effect of surface roughness will be analyzed in Section 3.4.

3.2.1. Mathematical Derivation. To calculate Q_{smooth}, it is necessary to calculate the power stored within the cavity (P_{stored}) and the power dissipated in the conductive cavity walls through ohmic loss (P_{smooth}). This can be represented mathematically as

$$Q_{smooth} = \frac{P_{stored}}{P_{smooth}} = \frac{\omega W_{total}}{P_{smooth}} \tag{58}$$

where W_{total} is given by (46).

The power dissipated in the conductive walls, P_{smooth}, can be found by [5]

$$P_{smooth} = \frac{R_s}{2}\int_{walls} |\mathbf{J}_s|^2 dS = \frac{R_s}{2}\int_{walls} |\mathbf{H}_{tan}|^2 dS \tag{59}$$

where R_s is the frequency dependent surface resistivity given by (60), $\mathbf{J_s}$ is the surface current vector, and $\mathbf{H}_{tan}$ is the tangential element of the magnetic field at the wall's surface.

$$R_s = \sqrt{\frac{\omega\mu_0}{2\sigma_c}} \tag{60}$$

Integrating over the walls, (59) becomes

$$\begin{aligned} P_{smooth} = \frac{R_s}{2}\Bigg\{ & 2\int_{y=0}^{b}\int_{x=0}^{a} |H_x|_{z=0}^2 dxdy + 2\int_{z=0}^{d}\int_{y=0}^{b} |H_z|_{x=0}^2 dydz \\ & + 2\int_{z=0}^{d}\int_{x=0}^{a} \left[|H_x|_{y=0}^2 + |H_z|_{y=0}^2\right] dxdz \Bigg\} \end{aligned} \tag{61}$$

Because $\beta_y = 0$ in a planar cavity and only the TE$_{m0\ell}$ modes are considered, the only non-zero magnetic field components of (41) are H_x and H_z. Combining (61) and (41) gives

$$P_{smooth} = R_s \Bigg\{ \left(\frac{m\ell\pi^2 A_{m0\ell}}{ad\omega\mu_d\epsilon_d'}\right)^2 \int_{y=0}^{b}\int_{x=0}^{a} \sin^2\left(\frac{m\pi}{a}x\right) dxdy$$
$$+ \left[\frac{A_{mn\ell}}{\omega\mu_d\epsilon_d'}\left(\frac{m\pi}{a}\right)^2\right]^2 \int_{z=0}^{d}\int_{y=0}^{b} \sin^2\left(\frac{\ell\pi}{d}z\right) dydz$$
$$+ \left(\frac{m\ell\pi^2 A_{mn\ell}}{ad\omega\mu_d\epsilon_d'}\right)^2 \int_{z=0}^{d}\int_{x=0}^{a} \sin^2\left(\frac{m\pi}{a}x\right)\cos^2\left(\frac{\ell\pi}{d}z\right) dxdz \tag{62}$$
$$+ \left[\frac{A_{mn\ell}}{\omega\mu_d\epsilon_d'}\left(\frac{m\pi}{a}\right)^2\right]^2 \int_{z=0}^{d}\int_{x=0}^{a} \cos\left(\frac{m\pi}{a}x\right)\sin\left(\frac{\ell\pi}{d}z\right) dxdz \Bigg\}$$

Solving the integrals in (62) results in an expression for smooth conductor loss in a $\mathrm{TE}_{m0\ell}$ rectangular cavity.

$$P_{smooth} = \frac{R_s}{4}\left(\frac{A_{m0l}}{\omega\mu_d\epsilon_d}\right)^2\left(\frac{m\pi^2}{a^2 d}\right)^2 (\ell^2 a^{3d} + m^2 ad^3 + 2\ell^2 a^3 b + 2m^2 bd^3) \tag{63}$$

Substituting (46) and (63) into (58) gives the smooth conductor Q-factor for a $\mathrm{TE}_{m0\ell}$ rectangular cavity.

$$Q_{smooth} = \frac{2\omega \frac{A_{m0\ell}^2}{\epsilon_d}\left(\frac{m\pi}{a}\right)^2 \frac{abd}{16}}{\frac{R_s}{4}\left(\frac{A_{m0l}}{\omega\mu_d\epsilon_d}\right)^2\left(\frac{m\pi^2}{a^2 d}\right)^2 (\ell^2 a^{3d} + m^2 ad^3 + 2\ell^2 a^3 b + 2m^2 bd^3)} \tag{64}$$

Simplifying, (64) becomes

$$Q_{smooth} = \frac{4\pi f^3 \epsilon_d \mu_d^2 a^3 bd^3}{R_s(\ell^2 a^3 d + m^2 ad^3 + 2\ell^2 a^3 b + 2m^2 bd^3)} \tag{65}$$

For analysis purposes, it may be useful to compare the relative contributions of a cavity's side walls and top/bottom walls to the total Q-factor given in (65). Breaking (61) into two separate equations results in

$$P_{TB} = R_s \int_{z=0}^{d} \int_{x=0}^{a} \left[|H_x|_{y=0}^2 + |H_z|_{y=0}^2 \right] dxdz \tag{66}$$

and

$$P_{sides} = R_s \left(2 \int_{y=0}^{b} \int_{x=0}^{a} |H_x|_{z=0}^2 dxdy + 2 \int_{z=0}^{d} \int_{y=0}^{b} |H_z|_{x=0}^2 dydz \right) \tag{67}$$

where P_{TB} is the power lost on the top and bottom walls, and P_{sides} is the power lost on the other four sides. Calculating the Q-factors for P_{TB} and P_{sides} results in

$$Q_{TB} = \frac{\omega^3 a^2 b d^2 \mu_d^2 \epsilon_d'}{2\pi^2 R_s (\ell^2 a^2 + m^2 d^2)} \tag{68}$$

and

$$Q_{sides} = \frac{\omega^3 a^3 d^3 \mu_d^2 \epsilon_d'}{4\pi^2 R_s (\ell^2 a^3 + m^2 d^3)} \tag{69}$$

3.2.2. Analysis. Because the conductor Q-factor of a cavity is heavily dependent upon the cavity dimensions and wall material, (65), (68), and (69) are best analyzed by modelling a representative example cavity. Q_{smooth} at the first 15 resonant modes of a vacuum-filled, copper-walled 40x50x1 mm cavity is shown in Figure 3.3. If this cavity were to be filled with a lossy dielectric material, then in the absence of other losses, the measured Q-factor of the cavity is represented by

$$\frac{1}{Q_m} = \frac{1}{Q_d} + \frac{1}{Q_{smooth}} \tag{70}$$

If Q_{smooth} is neglected in (70), the resulting error in measuring Q_d is shown in Figure 3.4 as a function of $\tan(\delta_d)$. This figure clearly indicates that error caused by neglecting Q_{smooth} in measuring low values of dielectric loss will be much greater than the error present in measurements of more lossy dielectrics. The error in measuring the dissipation factor of Rogers 4350 is approximately 35%, while the error with FR-4 is only 5%. It is important to note that the specific Q_{smooth} values and error percentages shown in these plots are only valid for the specific cavity used in this example. Nevertheless, the example cavity shows that neglecting Q_{smooth} results in very significant error in measured $\tan(\delta_d)$ for low loss materials.

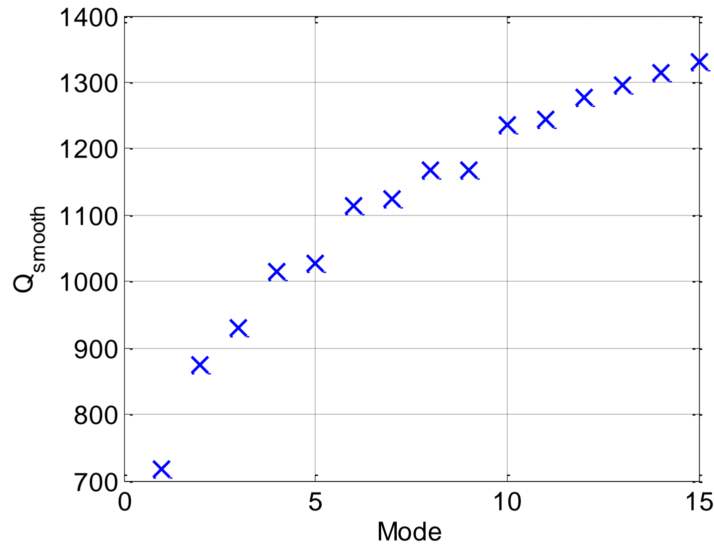

Figure 3.3. Calculated Q_{smooth} of the first 15 resonant modes of an example cavity

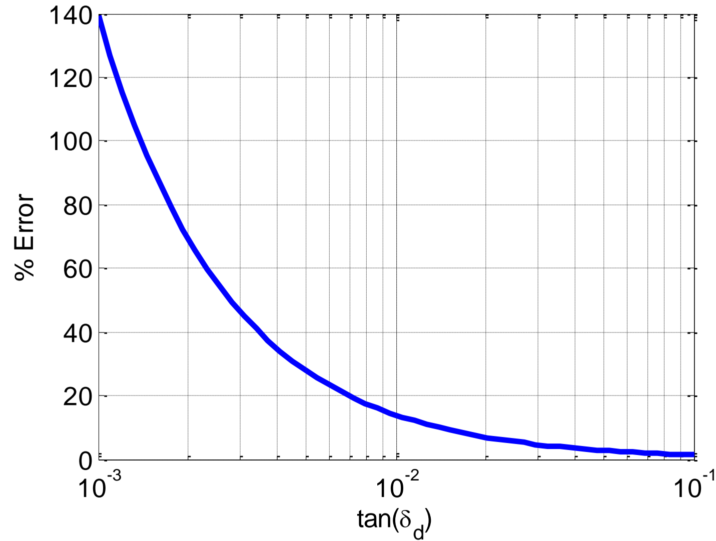

Figure 3.4. Error in measured $\tan(\delta_d)$ caused by neglecting Q_{smooth} in an example cavity

The expressions given in (68) and (69) provide the relative contributions of the top/bottom and side cavity walls to the total Q_{smooth}, respectively. The influence of each group of walls on Q_{smooth} as a function of b is shown in Figure 3.5 for a vacuum-filled 50x40xb mm cavity. Once again, the exact percentages presented in Figure 3.5 are only valid for this particular cavity; however, the fact remains that for any practical planar cavity where $a, d \gg b$, the top and bottom walls have substantially greater influence on Q_{smooth} than do the side walls.

The low influence of the side walls on Q_{smooth} has important implications for measuring practical cavities. Because of the way that PCBs are manufactured, the side wall conductors are likely to be constructed using a different process than the top and bottom layers. This manufacturing difference can lead to different values of σ_c and surface roughness (discussed in Section 3.4) for the side walls. Fortunately, small differences in the properties of the side walls will have very little impact on the total value of Q_{smooth} because the cavity's power loss is dominated by the top and bottom walls.

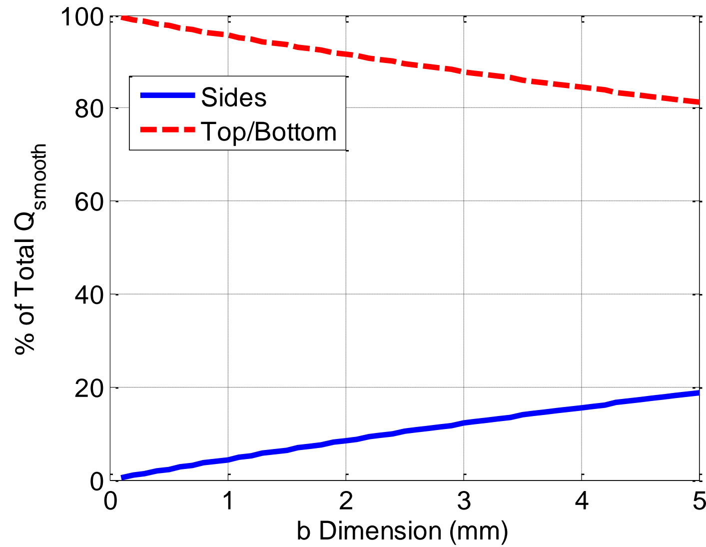

Figure 3.5. Relative influence of the side walls and top/bottom walls of a 50x40xb mm cavity on the total Q factor at the fundamental mode

3.3. EFFECT OF SURFACE CONDUCTIVITY ON FREQUENCY

The inductive surface impedance of the cavity walls causes a phase shift in the internal standing waves, resulting in a change in resonant frequency. This shift in resonance must be accounted for through mathematical corrections to (25).

3.3.1. Mathematical Derivation. The approach of [7] is first used to find the relationship between attenuation constant, α, and propagation constant, β_z, of a rectangular waveguide operating in the TE_{10} mode. This relationship is then extended to cavity resonators to find a proportionality between Q_{smooth} and resonant frequency. It is assumed that all cavity walls are made of homogeneous, isotropic conductors with identical values of conductivity.

The propagation constant of a waveguide is given by

$$\gamma_0 = \alpha_0 + j\beta_z \tag{71}$$

Because $\alpha_0 = 0$ for an ideal waveguide,

$$\beta_z = -j\gamma_0 \tag{72}$$

The cutoff wavenumber, β_c, is defined by

$$\beta_c^2 = \beta_x^2 + \beta_y^2 \tag{73}$$

β_c and β_z are related by

$$\beta_0^2 = \left(\omega\sqrt{\mu_d \epsilon_d'}\right)^2 = \beta_c^2 + \beta_z^2 = \beta_c^2 - \gamma_0^2 \tag{74}$$

Thus,

$$\gamma^2 = \beta_c^2 - \beta_0^2 \tag{75}$$

In an ideal, lossless waveguide, $E_y = 0$ at the $x = a$ wall because of the PEC boundary condition. In a non-ideal cavity, however, the finite skin depth causes some amount of field penetration into the walls. This penetration is represented by adding small Δ terms to the directional wavenumbers and propagation constant.

$$\begin{cases} \beta_x = \beta_{x0} + \Delta\beta_x \\ \beta_y = \beta_{y0} + \Delta\beta_y \\ \beta_z = \beta_{z0} + \Delta\beta_z \\ \beta_c = \beta_{c0} + \Delta\beta_c \\ \gamma = \gamma_0 + \Delta\gamma \end{cases} \tag{76}$$

where

$$\Delta\gamma = \alpha + j\Delta\beta_z \tag{77}$$

Applying (76) to (75) results in

$$(\gamma + \Delta\gamma)^2 = (\beta_c + \Delta\beta_c)^2 - \beta_0^2 \tag{78}$$

Evaluating (78), neglecting all squared Δ terms, and solving for $\Delta\gamma$ results in

$$\Delta\gamma = \frac{(\Delta\beta_c)(\beta_c)}{j\beta_z} \tag{79}$$

Because $\beta_y \cong 0$ in the TE_{10} mode,

$$\beta_c = \beta_x \tag{80}$$

Thus,

$$\Delta\gamma = \frac{(\Delta\beta_x)(\beta_x)}{j\beta_z} \tag{81}$$

It is now necessary to relate the surface impedance of the wall, Z_s, to $\Delta\beta_x$. The surface impedance of the wall at $x = a$ is given by

$$Z_s = \left.\frac{E_y}{H_z}\right|_{x=a} = \frac{\frac{\beta_x}{\epsilon_d'} A_{mn\ell} \sin(\beta_x x)\cos(\beta_y y)\sin(\beta_z z)}{\frac{jA_{mn\ell}}{\omega_0 \mu_d \epsilon_d'}\left(\beta_x^2 + \beta_y^2\right)\cos(\beta_x x)\cos(\beta_y y)\sin(\beta_z z)} \tag{82}$$

which reduces to

$$\left.\frac{E_y}{H_z}\right|_{x=a} = \frac{\omega_0 \mu_d \sin(m\pi + \Delta\beta_x a)}{j(\beta_x + \Delta\beta_x)\cos(m\pi + \Delta\beta_x a)} \tag{83}$$

Because $\sin(m\pi + u) = \sin(u)$, (83) further reduces to

$$\left.\frac{E_y}{H_z}\right|_{x=a} = \frac{\omega_0 \mu_d}{j(\beta_x + \Delta\beta_x)} \tan(\Delta\beta_x a) \tag{84}$$

If it is assumed that $(\Delta\beta_x a)$ is small, then $\tan(\Delta\beta_x a) = \Delta\beta_x a$. Thus,

$$\left.\frac{E_y}{H_z}\right|_{x=a} = \frac{\omega_0 \mu_d \Delta\beta_x a}{j(\beta_x + \Delta\beta_x)} = Z_s \tag{85}$$

Assuming $\beta_x \gg \Delta\beta_x$ in the denominator,

$$\left.\frac{E_y}{H_z}\right|_{x=a} = \frac{\omega_0 \mu_d \Delta\beta_x a}{j(\beta_x)} = Z_s \tag{86}$$

Solving for $\Delta\beta_x$,

$$\Delta\beta_x = \frac{j\beta_x}{a\omega_0 \mu_d} Z_s \tag{87}$$

Substituting (87) into (81) results in

$$\Delta\gamma = \alpha + j\Delta\beta_z = GZ_s = G(R_s + jX_s) \tag{88}$$

where G is a lumped constant value. Thus,

$$\frac{\Delta\beta_z}{\alpha} = \frac{X_s}{R_s} \tag{89}$$

In a good conductor,

$$Z_s = R_s + jX_s = \sqrt{\frac{\omega\mu_0}{2\sigma_c}}(1 + j) \tag{90}$$

Thus, $X_s = R_s$ and

$$\alpha = \Delta\beta_z \tag{91}$$

In a waveguide, γ is a function of z because the internal wave is travelling along the z-axis. In a cavity, however, only standing waves exist. It makes more sense, then, for γ in a cavity to be a function of time and frequency rather than of distance and phase. The two forms of γ are related by the phase velocity, v_p.

$$e^{-\gamma z} = e^{-[\alpha + j(\beta_z + \Delta\beta_z)]z} = e^{-[\alpha_t + j(\omega_0 + \Delta\omega)](t/v_p)} \tag{92}$$

where α_t is the time-domain attenuation constant and $\Delta\omega$ is the shift in resonant frequency due to wall impedance. Comparing the real and imaginary parts of the two forms of γ reveals that

$$\Delta\omega = \alpha_t \tag{93}$$

It is known that α_t and Q_c are related by [8]

$$Q_{smooth} = \frac{\omega_0}{2\alpha_t} \tag{94}$$

Thus,

$$\Delta\omega = \frac{\omega_0}{2Q_{smooth}} \tag{95}$$

which is same result derived by eigenmode analysis in [8].

Applying the compensation given in (95) to (57) results in an expression for resonate frequency that has been compensated for both dielectric loss and wall reactance.

$$f_r = \frac{\left(1 - \frac{1}{2Q_{smooth}}\right)\sqrt{\left(\frac{m\pi}{a}\right)^2 + \left(\frac{n\pi}{b}\right)^2 + \left(\frac{\ell\pi}{d}\right)^2}}{2\pi\sqrt{\mu_d \epsilon'_d}\sqrt{\frac{1}{2}\left(\sqrt{1+\tan^2(\delta_d)}+1\right)}} \tag{96}$$

3.3.2. Analysis. The expression for resonant frequency shift given in (96) is mostly easily analyzed by using the results for Q_{smooth} that were determined in Section 3.2.2 for a 50x40x1 mm cavity filled with a lossless dielectric with $\epsilon'_r = 3.66$. As $Q_{smooth} \to \infty$, the frequency predicted by (96) approaches f_{ideal}, as shown in Figure 3.6. The resonant frequency begins to measurably decrease as σ_c is lowered to more practical values. For copper ($\sigma_c = 5.8 \times 10^7\ S/m$), this results in a 0.05% change in resonant frequency (see Figure 3.7). The error in measured ϵ' caused by this resonant shift is plotted in Figure 3.8. According to this figure, copper walls will cause an error of 0.14% in measured ϵ' at the fundamental mode. Figure 3.3 indicates that Q_c increases at higher order modes. It is then expected that the relative change in resonant frequency—and error in measured ϵ'—will decrease at higher modes. This is confirmed in Figure 3.9.

While an error in ϵ' of 0.14% is an order of magnitude greater than the error caused by dielectric loss, the error due to wall reactance is still negligible in most cases. While this error would be measurable in a system with perfect cavity coupling and instrument calibration, the reality is that larger sources of error will dominate.

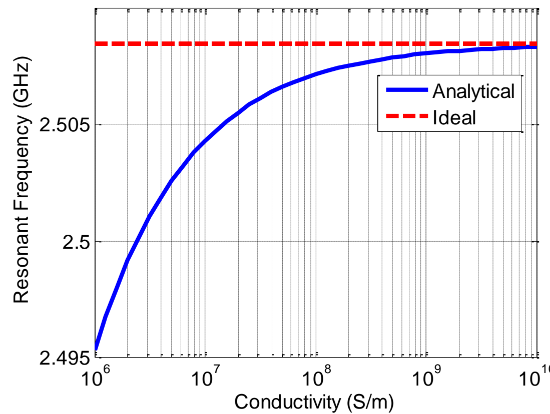

Figure 3.6. Resonant frequency of a TE_{101} example cavity as a function of σ_c

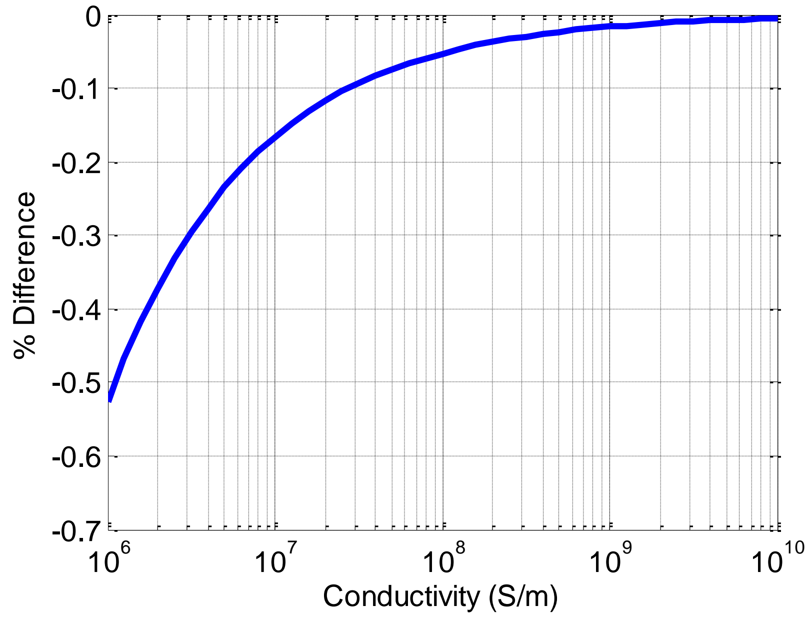

Figure 3.7. Change in resonant frequency of a TE_{101} example cavity as a function of σ_c

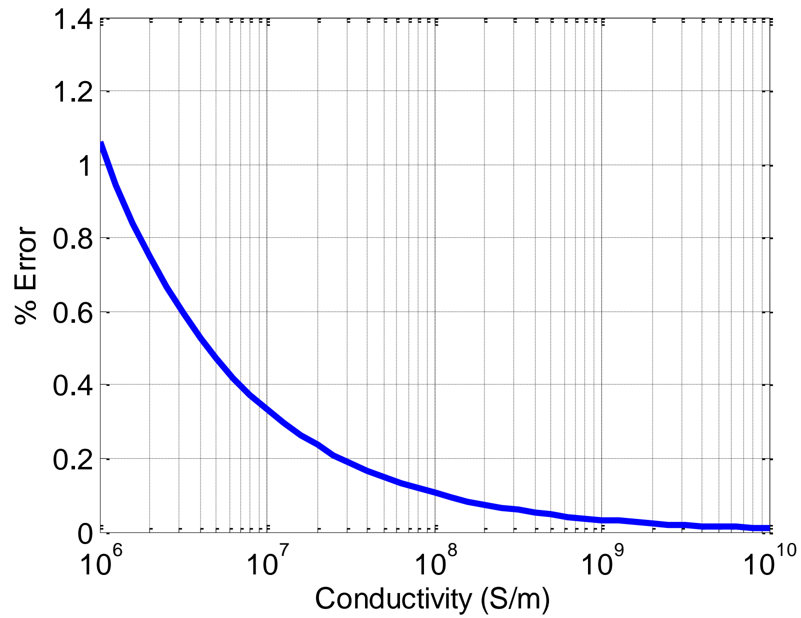

Figure 3.8. Error in permittivity measurement caused by neglecting finite wall conductivity in a TE_{101} example cavity as a function of σ_c

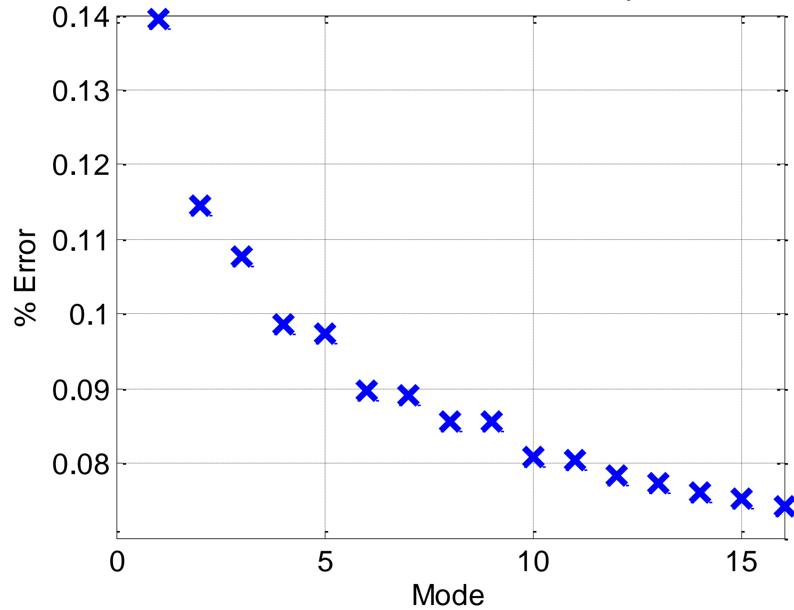

Figure 3.9. Error in permittivity measurement caused by neglecting finite wall conductivity in an example cavity as a function of resonant mode

3.4. EFFECT OF CONDUCTOR SURFACE ROUGHNESS ON Q-FACTOR

As printed circuit boards began to be used at increasing high frequencies, designers and researches alike noticed that transmission lines exhibited greater insertion loss than that predicted by the $\sqrt{f}$ behavior of the skin effect. This increase in loss was found to be caused by conductor surface roughness [9] [10]. The copper sheets used in PCB manufacturing are chemically roughened by the manufacturer to improve adhesion to the PCB substrate, as shown in Figure 3.10. The roughness is usually specified in RMS µm height, and typical values range from 0.5-3 μm_{RMS} [11]. The surface roughness loss becomes substantial when skin depth is comparable to the roughness height.

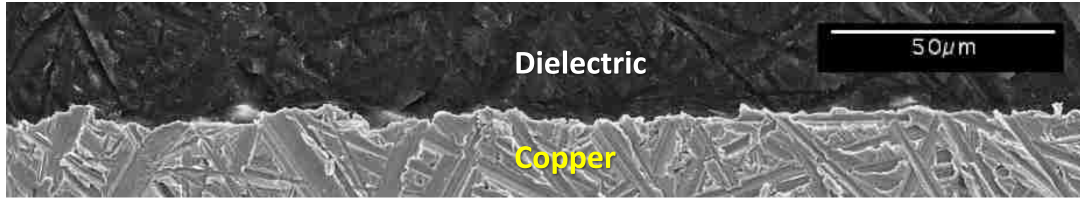

Figure 3.10. Cross sectional image of conductor surface roughness

It has been traditionally believed that the increase in conductor loss is due to an increase in the length the current must travel along the edge of the rough surface. Recent publications, however, have questioned this belief. If the roughness loss were indeed due to increased current path length, then it is expected that a corresponding increase in propagation time and phase constant would be present. Such an increase in phase is not observed experimentally [12]. A more accurate approach to understanding surface roughness loss is to model the conductor surface as a network of spheroids, each scattering and absorbing a portion of the incident wave [12] [13].

To accurately characterize the dissipation factor of a dielectric material using cavity resonance, it is necessary to account for the effect of surface roughness on the Q-factor of the cavity. Three techniques for approximating the effect of surface roughness are investigated in this thesis, each with differing levels of accuracy and complexity. All three methods calculate a roughness coefficient ξ such that

$$P_c = \xi P_{smooth} \tag{97}$$

where P_c is the total conductor loss, including roughness loss. This expression can be written in terms of Q-factor as

$$\mathrm{Q_c} = \frac{Q_{smooth}}{\xi} = \left(\frac{1}{Q_{smooth}} + \frac{1}{Q_{rough}}\right)^{-1} \tag{98}$$

where Q_c is the total conductor Q-factor.

3.4.1. Hammerstad-Jensen Model. The most common method to calculate ξ is the Hammerstad-Jensen model, given by

$$\xi_{HJ} = 1 + \frac{2}{\pi}\tan^{-1}\left[1.4\left(\frac{h_{RMS}}{\delta}\right)^2\right] \tag{99}$$

where δ is the skin depth and h_{RMS} is the RMS inclusion height [9]. This model was developed as an empirical fit to the results calculated in [14] that assumed a triangular roughness profile seen in Figure 3.11.

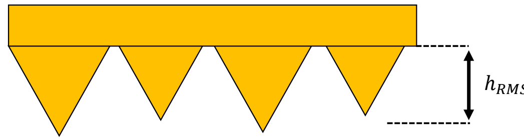

Figure 3.11. Surface profile assumed by the Hammerstad-Jensen model

The Hammerstad-Jensen model requires only one surface parameter, h_{RMS}, which is often provided by manufacturers of PCB material. The easy availability of the needed parameter makes the Hammerstad-Jensen model extremely easy to use in practice. The accuracy of this model, however, has been found to be quite poor at higher frequencies. The formula given in (99) saturates at a value of 2, even though no physical saturation of loss has been observed to occur under 50 GHz. This model's usefulness is generally limited to 2-3 GHz, where it is found to be reasonably accurate for small-to-moderate values of h_{RMS} [12].

3.4.2. Hall Hemispherical Model. The Hall Hemispherical model [13] treats the rough conductor surface as a series of hemispheroids of height h_{RMS}, width B_{RMS}, and spacing s_{RMS}, as shown in Figure 3.12. Each hemispheroid base area A_{base} is assumed to be sitting alone on a flat square conductive tile of area A_{tile} as illustrated in Figure 3.13.

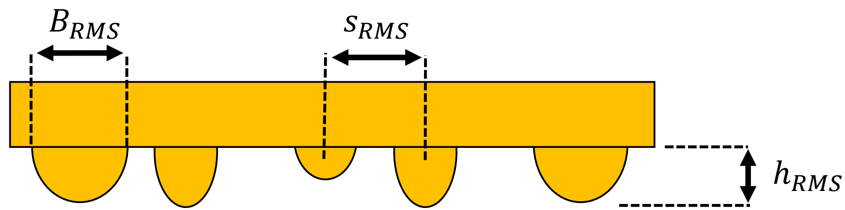

Figure 3.12. Surface profile assumed by the Hall Hemispherical model

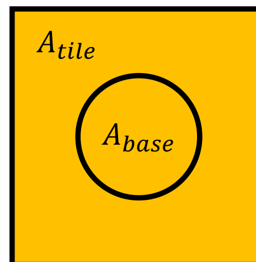

Figure 3.13. Top view of the surface profile assumed by the Hall Hemispherical model

The power scattered and absorbed by the hemispheroid is found by calculating the scattering coefficients for an equivalent sphere with the same surface area as the hemispheroid. The resulting power loss is divided by 2 to account for the fact that only half the sphere physically exists. The power lost in the smooth plane surrounding the hemispheroid is then added. The overall expression for power loss in the hemispheroid

and surrounding plane is normalized against the power loss over a smooth plane with no hemisphere. The resulting expression for the roughness coefficient is

$$\xi_{hemi} = \frac{\left(\left| Re\left[\sqrt{\frac{\mu_d}{\epsilon_d'}} \frac{3\pi}{4\beta_0^2} (u + v) \right] \right| + \frac{\mu_0 \omega \delta}{4} (A_{tile} - A_{base}) \right)}{\frac{\mu_0 \omega \delta}{4} A_{tile}} \tag{100}$$

where u and v are the scattering coefficients for a sphere, given by

$$u = -\frac{2j}{3} (\beta_0 r_e)^3 \left[\frac{1 - \frac{\delta}{r_e}(1 + j)}{1 + \frac{\delta}{2r_e}(1 + j)} \right] \tag{101}$$

$$v = -\frac{2j}{3} (\beta_0 r_e)^3 \left[\frac{1 - \left(\frac{4j}{\beta_0^2 r_e \delta} \right) \left(\frac{1}{1 - j} \right)}{1 + \left(\frac{2j}{\beta_0^2 r_e \delta} \right) \left(\frac{1}{1 - j} \right)} \right] \tag{102}$$

The values of A_{tile} and $A_{base}$are related to the RMS inclusion spacing and base width, respectively:

$$A_{tile} = s_{RMS}^2 \tag{103}$$

$$A_{base} = \pi \left(\frac{B_{RMS}}{2} \right)^2 \tag{104}$$

Finally, the equivalent radius of a sphere having the same surface area as the hemispheroid is calculated by

$$r_e = \sqrt[3]{h_{RMS} \left(\frac{B_{RMS}}{2} \right)^2} \tag{105}$$

At low frequencies, ξ_{hemi} is a fractional value, which implies lower loss than that of a perfectly smooth conductor, which is clearly invalid. This error is corrected by setting the roughness coefficient to unity at frequencies where the power lost in the hemispheroid is less than the power lost in a plane of equivalent base area.

$$\xi = \begin{cases} 1, & \xi_{hemi} \leq 1 \\ \xi_{hemi}, & \xi_{hemi} > 1 \end{cases} \tag{106}$$

The Hall Hemispherical model requires three statistical measurements of the conductor surface. This data is not typically supplied by manufacturers, but can be measured by analyzing a two-dimensional cross section by scanning electron microscope or optical microscope. Experimental testing has shown that the Hall model is valid at frequencies of at least 20 GHz [13].

3.4.3. Huray Snowball Model. The Huray "Snowball" model [12] is similar to the Hall Hemispherical model in that it treats the conductor surface roughness as a series of spherical protrusions. Unlike the Hall method, however, which represents each inclusion as a single hemispheroid, the Huray model analyzes each inclusions as a pyramidal stack of conductive spheres, or "snowballs," of different radii. This is illustrated in Figure 3.14.

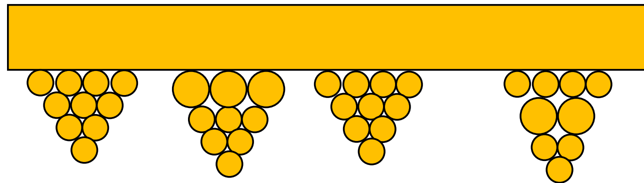

Figure 3.14. Surface profile assumed by the Huray Snowball model

The power scattered and absorbed by each snowball is calculated and summed together. An additional loss term is included that accounts for the thickness variation of the foil without the stacks of spheres. Thickness variation results in a somewhat "wavy" appearance and a corresponding increase in surface area and is present even before the conductor surface has been chemically roughened. The final formula for the roughness coefficient is

$$\xi_{SB} = \frac{A_{Matte}}{A_{Flat}} + 6\sum_{i}\left[\frac{\left(\frac{N_i \pi r_i^2}{A_{Flat}}\right)}{1 + \frac{\delta}{r_i} + \frac{\delta^2}{2r_i^2}}\right] \tag{107}$$

where A_{matte} is the surface area of the foil before being chemically roughened and A_{flat} is the geometrical area of the foil when projected onto a flat plane. N_i is the number of spheres over the foil's surface area of radius r_i.

The expression for ξ_{SB} looks deceptively simple. While easy to calculate mathematically, ξ_{SB} requires the parameters A_{Matte}, N_i, and r_i, which are not trivial to measure. A surface profilometry scan is needed both before and after chemical roughening, which limits the use of the Huray method to manufacturers who have access to the foil at various stages during the production process before lamination. This usage limitation is unfortunate, as the model has been shown to be accurate to at least 50 GHz [12].

3.4.4. Analysis. The three surface roughness models analyzed above can be used interchangeably, since they are simply different methods of calculating the same coefficient. For most uses in dielectric characterization, however, the Hall Hemispherical model provides the best tradeoff between complexity and accuracy. If it is not possible to make the cross-sectional images required to calculate the parameters for the Hall model, the Hammerstad model may be used with manufacturer-provided parameters. The Hammerstad model will result in decreased accuracy in calculated $\tan(\delta_d)$ when compared to the Hall model, but will still provide an improvement over measurements in which the surface roughness is neglected altogether.

To analyze the effect of surface roughness on a cavity's Q-factor, the hemispherical roughness parameters from [13] of $h_{RMS} = 5.8\ \mu m$, $s_{RMS} = 9.4\ \mu m$ were used to calculate the roughness factor. The data in [13] did not list the value of B_{RMS}, which was assumed here to be 5.0 μm. The calculated values of ξ over frequency for a cavity filled with $\epsilon_r' = 3.66$ is shown in Figure 3.15. The Q-factor of a 50x40x1 mm cavity is compared between a cavity with rough and smooth walls in Figure 3.16. The surface roughness results in a decrease in Q_c, as expected. The rate of change of roughness loss with respect to frequency, $\frac{d\xi}{df}$, is less than $\frac{dQ_{smooth}}{df}$, meaning that even when surface roughness is included in the model, Q_c still increases with frequency. The implications of this Q-factor increase lead to a somewhat unexpected conclusion—the presence of surface roughness in a cavity becomes increasingly less relevant to dielectric measurement at high frequencies. To illustrate this, the measured error in $\tan(\delta_d)$ caused by neglecting surface roughness is plotted in Figure 3.29 as a function of dissipation factor and frequency. A frequency dependence, albeit a somewhat small dependence, is seen in the error. The absolute values of error shown in this plot are highly dependent upon the cavity geometry, surface roughness profile, and value of ϵ_r'. From the error seen in this example cavity, however, it can be expected that for low loss materials, the error caused by surface roughness is in the order of 25%.

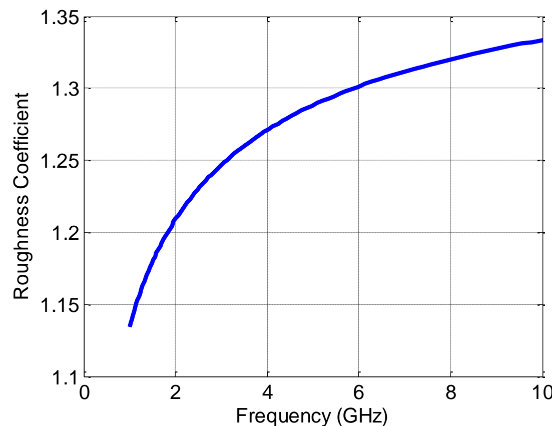

Figure 3.15. Calculated roughness coefficient for $h_{RMS} = 5.8\ \mu m$, $s_{RMS} = 9.4\ \mu m$, and of $B_{RMS} = 5.0\ \mu m$

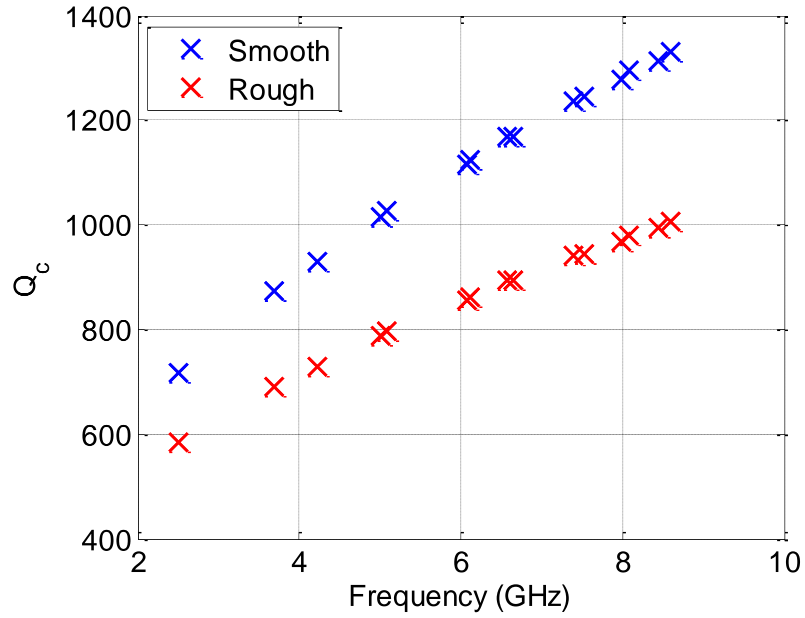

Figure 3.16. Comparison of Q-factor for smooth and rough conductors as a function of frequency

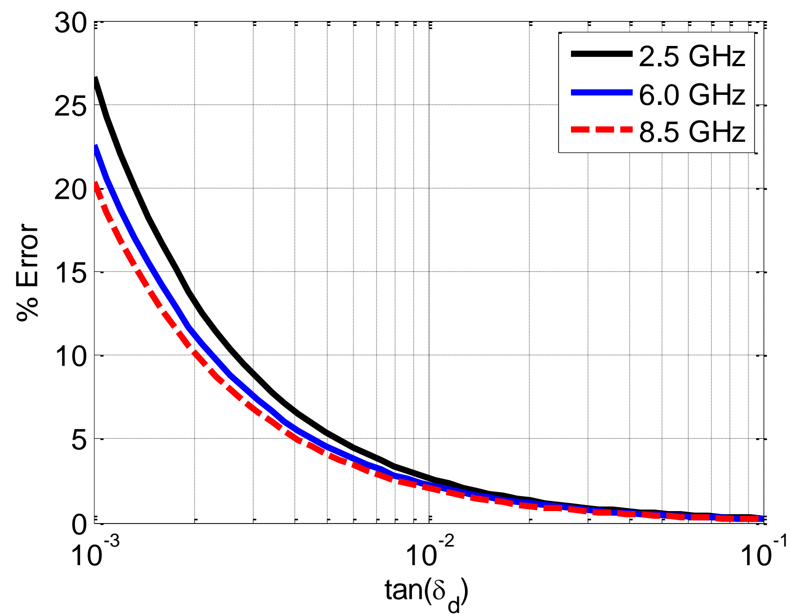

Figure 3.17. Error in measured dissipation factor due to surface roughness as a function of $\tan(\delta_d)$ for $\epsilon_r' = 3.66$ in a TE_{101} 50x40x1 mm cavity

3.5. EFFECT OF CAVITY COUPLING ON Q-FACTOR

The previous sections have focused on the effects of the non-ideal parameters of the cavity structure as if it was a closed system. In reality, however, a cavity must be excited by an outside circuit and coupling network. This coupling network can be modelled with the resonator as an equivalent circuit, as shown in Figure 3.18. Each resonant mode must be represented by a circuit with different component values. The real part of the external coupling impedance, g_e, will cause additional power loss, while the imaginary part of the external impedance, b_e, will cause frequency detuning.

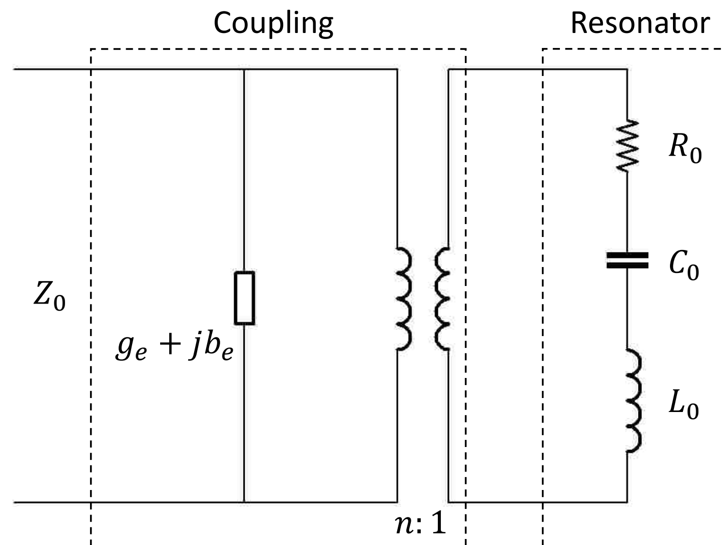

Figure 3.18. Equivalent circuit of a cavity resonator

3.5.1. Mathematical Derivation. To analyze the change in Q-factor as a result of the external loading, it is possible to neglect the reactive part of the coupling impedance and reflect the external resistance across the transformer. This simplified circuit is shown in Figure 3.19. In this circuit, the resonant frequency ω_0 is given by

$$\omega_0 = \frac{1}{\sqrt{C_0 L_0}} \tag{108}$$

The internal Q-factor, Q_{int}, represents all losses internal to the cavity, including Q_d (and dielectric dissipation factor by association). The external Q-factor, Q_{ext}, represents the power lost through the cavity coupling. Any quality factor measurement will include both Q_{int} and Q_{ext}. To accurately measure Q_d, it is therefore necessary to mathematically calculate and remove the value of Q_{ext}. Expressions for Q_{int} and Q_{ext} for the simplified equivalent circuit in Figure 3.19 are given by [5]

$$Q_{int} = \frac{1}{R_0}\sqrt{\frac{L_0}{C_0}} = \frac{\omega_0}{R_0} L_0 \tag{109}$$

$$Q_{ext} = \frac{1}{R_C}\sqrt{\frac{L_0}{C_0}} \tag{110}$$

It is now necessary to introduce the coupling coefficient, $\mathscr{k}$. This coefficient is ratio of the power lost in the coupling network to the power lost in the resonator.

$$\mathscr{k} = \frac{R_c}{R_0} = \frac{Q_{int}}{Q_{ext}} \tag{111}$$

If $\mathscr{k} > 1$, the resonator is considered overcoupled. If $\mathscr{k} < 1$, the resonator is undercoupled. If $\mathscr{k} = 1$, the resonator is said to be critically coupled. Observing the complex value of a resonator's S_{11} on a Smith chart quickly reveals whether the resonator is overcoupled, critically coupled, or undercoupled as shown in Figure 3.20. The resonance circle of an overcoupled resonator will encompass the origin of the chart, while the origin remains outside the resonance circle of an undercoupled system. At critical coupling, the resonance circle will pass through the origin. The value of $\mathscr{k}$ can be found by measuring $|S_{11}|$ at resonance.

$$\mathcal{k} = \begin{cases} \text{VSWR}, & \text{Overcoupled} \\ \dfrac{1}{\text{VSWR}}, & \text{Undercoupled} \end{cases} \tag{112}$$

where

$$\text{VSWR} = \frac{1 + |\text{S}_{11}|}{1 - |S_{11}|} \tag{113}$$

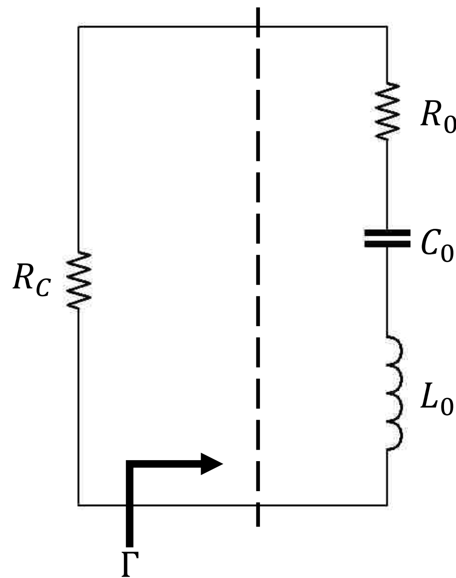

Figure 3.19. Simplified equivalent circuit of a cavity resonator

From Figure 3.19, the reflection coefficient looking from R_c into the cavity is given by

$$\Gamma = \frac{Z_L - Z_s}{Z_L + Z_s} = \frac{(R_0 - R_c) + j\left(\omega L_0 - \dfrac{1}{\omega C_0}\right)}{(R_0 + R_c) + j\left(\omega L_0 - \dfrac{1}{\omega C_0}\right)} \tag{114}$$

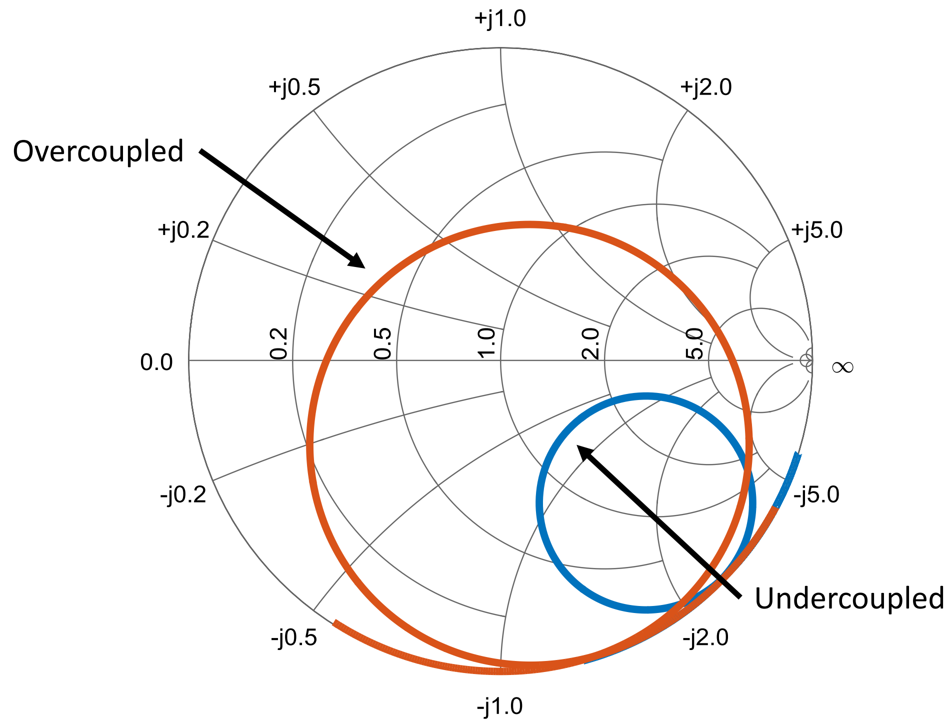

Figure 3.20. Smith chart representation of an overcoupled and undercoupled resonance

Substituting (109), (110), and (111) into (114) results in

$$\Gamma = \frac{(1 - k) + jQ_{int}\Omega}{(1 + k) + jQ_{int}\Omega} \tag{115}$$

where

$$\Omega = \frac{\omega}{\omega_0} - \frac{\omega_0}{\omega} \tag{116}$$

Near resonance, the value of Ω can be approximated as

$$\Omega \cong \frac{\Delta\omega_\rho}{\omega_0} = \frac{1}{Q_\rho} \tag{117}$$

where $\Delta\omega_\rho$ is the bandwidth at an arbitrary value of $\rho = |S_{11}|$ as shown in Figure 3.21. Q_ρ is the measured Q-factor at any value of ρ, but does not have any physical meaning by itself. It is, however, possible to write a mapping function $F(\rho, k) = Q_{int}/Q_\rho$ that uses the measured Q_ρ to determine Q_{int} and Q_{ext} [15]. To derive $F(\rho, k)$, it is first necessary to rewrite expression for Γ given in (114) as

$$\Gamma = \frac{(1 - k) + jF(\rho, k)}{(1 + k) + jF(\rho, k)} \tag{118}$$

Squaring the magnitude of (118),

$$\rho^2 = |\Gamma|^2 = \frac{(1 - k)^2 + F^2(\rho, k)}{(1 + k)^2 + F^2(\rho, k)} \tag{119}$$

Solving for $F(\rho, k)$,

$$F(\rho, k) = \sqrt{\frac{(1 + k)^2\rho^2 - (1 - k)^2}{(1 - \rho^2)}} \tag{120}$$

The mapping function $F(\rho, k)$ can be easily calculated by analyzing the measured reflection coefficient. The corrected value of Q_{int} is finally given by

$$Q_{int} = \frac{\Delta\omega_\rho}{\omega_0}\sqrt{\frac{(1 + k)^2\rho^2 - (1 - k)^2}{(1 - \rho^2)}} \tag{121}$$

Q_{ext} can be found by

$$Q_{ext} = \frac{Q_{int}}{k} \tag{122}$$

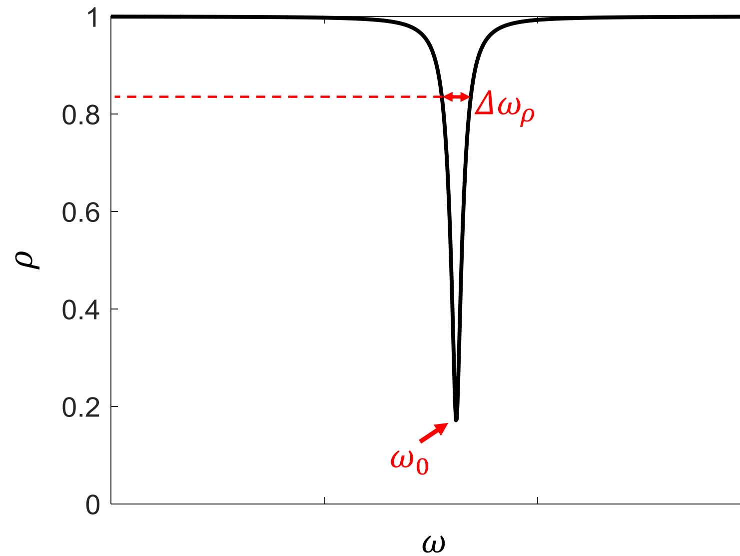

Figure 3.21. Graphical representation of $\Delta\omega_\rho$

3.5.2. Analysis. The effect of external loading on the measured Q-factor of a cavity cannot be easily analyzed without coupling data from a real or simulated resonance. Therefore, a CST model was built in which 50x40x1 mm cavity was fed by an SMA connector, as shown in Figure 3.22a. The cavity was filled with lossy Rogers 4350, the shell and center pin of the connector were modeled as PEC, and the connector dielectric material was lossy PTFE. A waveguide port provided the excitation for the simulation. The center pin of the SMA connector was extended into the cavity's dielectric, thus acting as a probe from which S_{11} could be measured. A cross-sectional image of the probe feed is shown in Figure 3.22b. The depth of probe penetration was varied from 0 mm to 0.9 mm to provide data with varying values of $\mathscr{k}$.

From each simulated $|S_{11}|$ curve, a corresponding value of $\mathscr{k}$ was calculated. The Smith chart representation of $|S_{11}|$ in Figure 3.23 was used to determine that four of the simulated resonances were undercoupled and two were overcoupled. Figure 3.24 shows the simulated $|S_{11}|$ data for each value of $\mathscr{k}$.

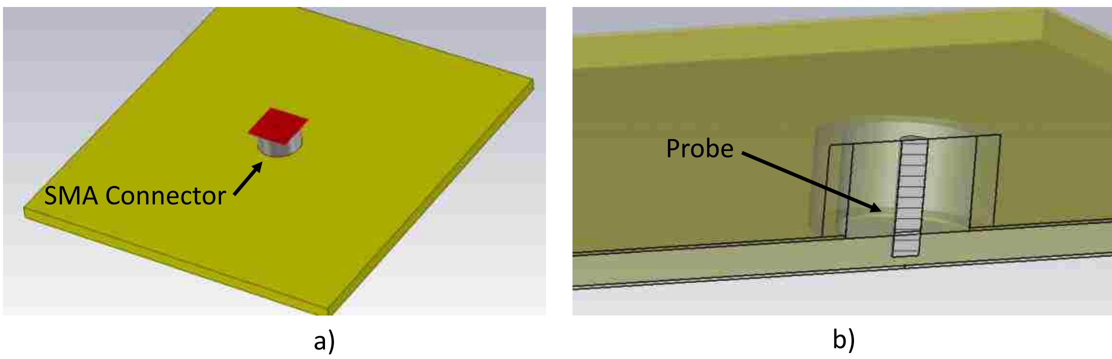

Figure 3.22. a) Image of the frequency-domain CST SMA-excitation model b) Cross-sectional image of the simulated cavity's SMA feed

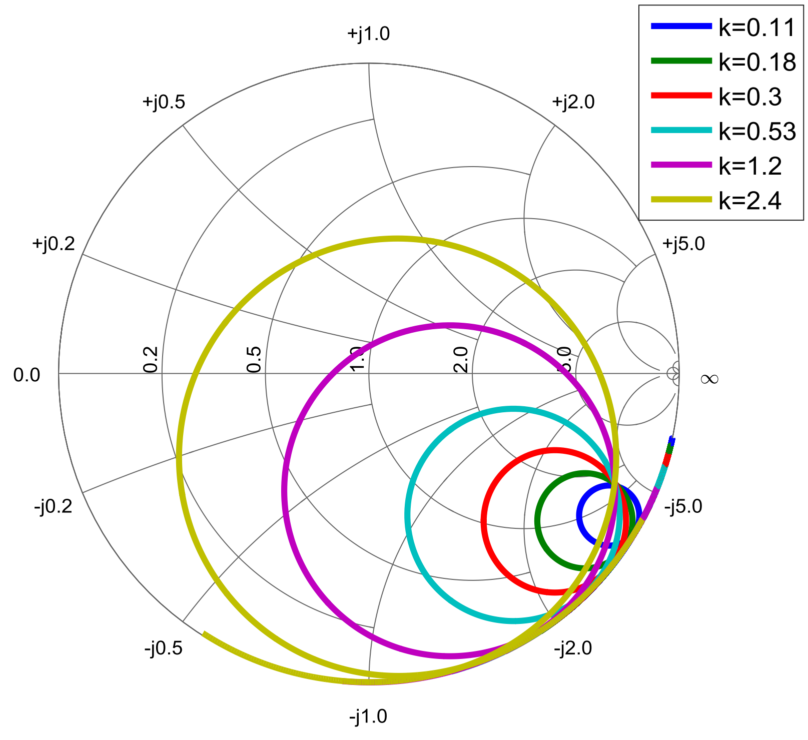

Figure 3.23. Smith chart representation of simulated $|S_{11}|$ results of a TE_{101} mode 50x40x1 mm cavity filled with Rogers 4350

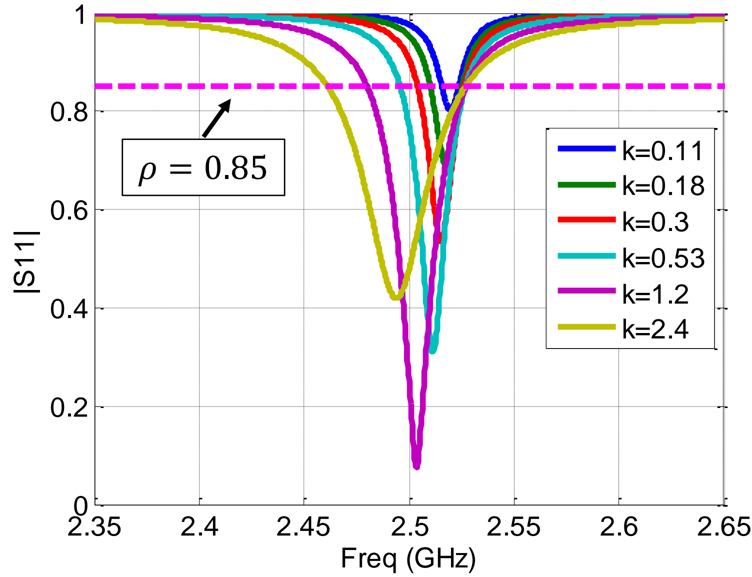

Figure 3.24. Simulated $|S_{11}|$ results of a TE_{101} mode 50x40x1 mm cavity filled with Rogers 4350

Because the value of $|S_{11}|$ at the resonance corresponding to $k = 0.11$ was 0.8, the value of ρ to be used in calculating Q_ρ was chosen to be 0.85. Any value of ρ greater than 0.8 could have been used, and lower values of ρ could have been used for the deeper resonances. For consistency, however, $\rho = 0.85$ was used for the calculation of Q_ρ for all simulated resonances. The resulting values of Q_ρ were then used to calculate Q_{int} and Q_{ext}. A loaded Q-factor, Q_L, was also calculated by

$$\frac{1}{Q_L} = \frac{1}{Q_{ext}} + \frac{1}{Q_{int}} \tag{123}$$

Figure 3.25 shows Q_{ext}, Q_{int}, and Q_L for each simulated value of k. In theory, Q_{int} is not affected by coupling conditions and should remain constant for all values of k. This is clearly seen in the data in Figure 3.25, where Q_{int} does not change with varying values of Q_{ext}. For large values of Q_{ext}, Q_L is very close to Q_{int}. As the external loading increases, however, Q_L begins to deviate greatly from Q_{int}. This

deviation will lead to errors in Q-factor measurement and thus in $\tan(\delta_d)$. The difference between Q_L and Q_{int} is shown in Figure 3.26. For an overcoupled cavity with $k = 2.4$, a difference of over 70% is seen. The difference is smaller for lower values of k, but will still lead to large errors in calculating $\tan(\delta_d)$. Figure 3.27 illustrates this point well, where it is shown that a coupling factor of only 0.3 will produce an error in $\tan(\delta_d)$ of nearly 50%. Errors in excess of 100% are present at the higher coupling factors. It is clear that the error in dissipation factor caused by neglecting Q_{ext} is not at all negligible.

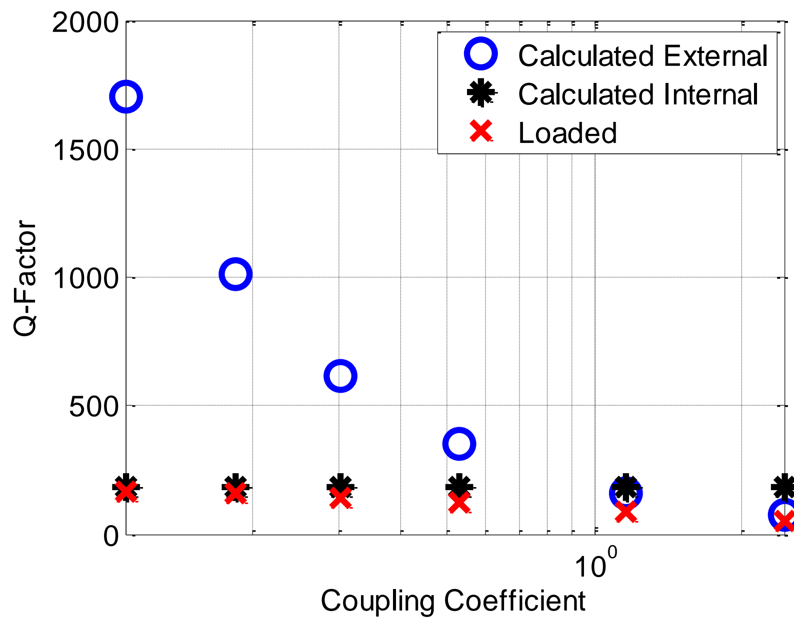

Figure 3.25. Calculated external, internal, and loaded Q-factors as a function of k for simulated data

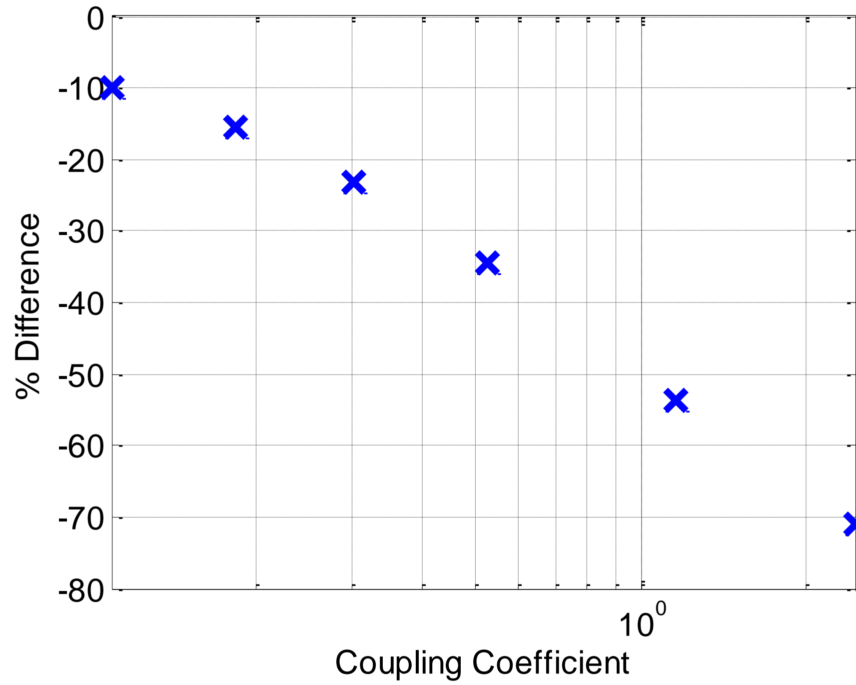

Figure 3.26. Difference between Q_{int} and Q_L as a function of $\mathscr{k}$

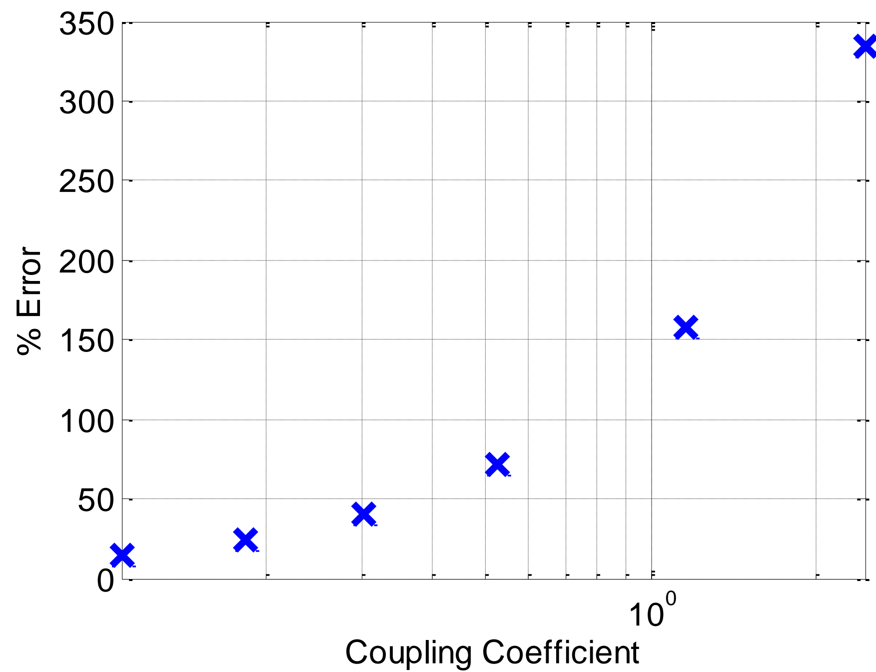

Figure 3.27. Error in calculated $\tan(\delta_d)$ caused by neglecting Q_{ext} as a function of $\mathscr{k}$

3.6. EFFECT OF COUPLING COEFFICIENT ON FREQUENCY

The reactive portion of the coupling impedance of the equivalent circuit in Figure 3.18 can cause detuning of the resonant frequency of a cavity. Most literature on the topic of cavity coupling focuses on the effect of coupling on Q-factor rather than resonant frequency, though there has been some successful research on the subject.

3.6.1. Empirical Method Development. It was found empirically in [16] that the relationship between loaded and unloaded resonant frequencies can be found by

$$f_L = \left(1 - \frac{A}{Q_{ext}^g}\right) f_u \tag{124}$$

where A and g are empirically determined constants. The constant A can take either positive or negative values, depending upon the direction of detuning. The authors of [16] propose a three-point measurement method to determine the constants and unloaded resonant frequency. Three separate resonance measurements must be made, each having a different coupling factor and external Q-factor. This means that either the coupling probe's position or length must be changed. The resulting system of equations

$$f_{L,i} = \left(1 - \frac{A}{Q_{ext,i}^g}\right) f_u, \quad i = 1,2,3 \tag{125}$$

can then be solved numerically for f_u using each measured value of f_L and Q_{ext}.

For dielectric measurement, physically moving a probe position or changing probe depth is highly impractical. If three cavities of identical size were produced, however, then each cavity could be made with a different coupling location. This three-cavity method would only work if the physical size of the cavities was controlled to a tight tolerance and if it is assumed that the dielectric properties of the material did not vary between the three cavities.

3.6.2. Analysis. To quantify the effect of coupling on frequency detuning, the resonant frequencies from the FEM simulation performed in Section 3.5.2 were compared to the unloaded resonant frequency calculated with (96) (which was also confirmed using an eigenmode simulation). The frequency difference caused by the reactive coupling network is plotted against k in Figure 3.28. The corresponding error in ϵ' measurement is shown in Figure 3.29. This permittivity error is on the order of 1% for the example 50x40x1 mm cavity operating in the TE_{101} mode. Comparison of the error caused by reactive coupling to the other sources of frequency error explored in this thesis reveals that the coupling error is likely to dominate (though this depends upon the coupling coefficient and cavity geometry).

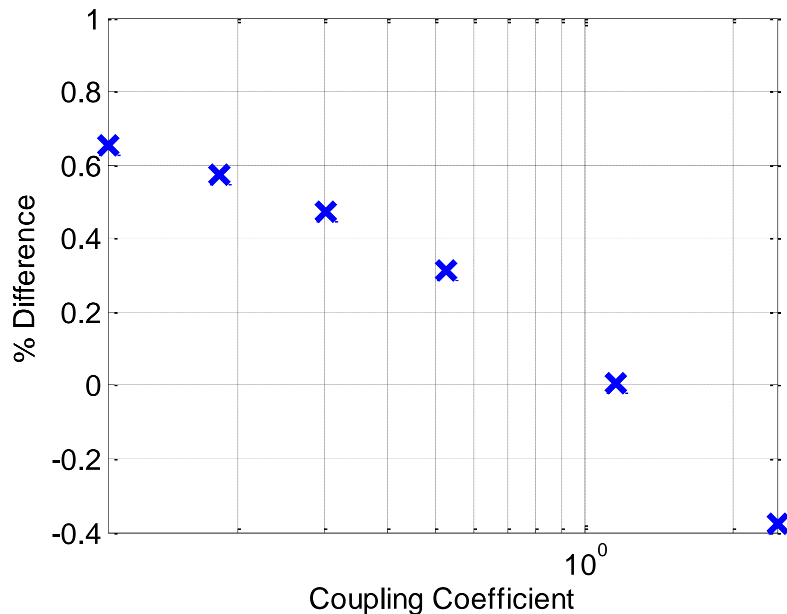

Figure 3.28. Shift in resonant frequency of a TE_{101} 50x40x1 mm cavity as a function of coupling coefficient

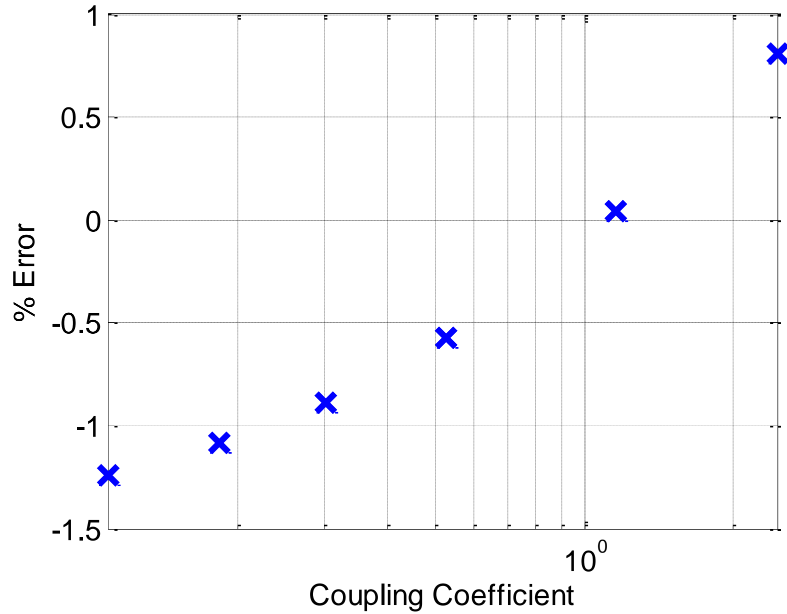

Figure 3.29. Error in calculated ϵ' in a TE_{101} 50x40x1 mm cavity as a function of coupling coefficient

Analysis of (124) reveals that for a given value and sign of A, the predicted resonant frequency shift can be in either the positive or negative direction. This suggests that as $Q_{ext} \rightarrow \infty$, the loaded resonant frequency should approach the unloaded resonant frequency. Though this limit intuitively seems reasonable, the simulated data in Figure 3.28 refutes this conclusion, as both positive and negative detuning is observed depending on the value of k. Repeated simulations of different geometries and materials have similar results. From these simulations, it appears that the empirical formula for determining the unloaded resonant frequency given in (124) is not applicable for planar cavities. Further research is required to adequately de-embed the reactive coupling network from the resonant frequency of a planar cavity.

3.7. DIELECTRIC CHARACTERIZATION PROCEDURE

A simple procedure based around the equations developed in Sections 3.1-3.6 can be used to determine the values of ϵ' and $\tan(\delta_d)$ of a dielectric material. A step-by-step outline of this procedure is presented below.

1. Design a rectangular cavity made of PCB laminate with an ideal resonant frequency close to the frequency of interest using (25) and the nominal material permittivity. It is possible to operate the cavity at higher order modes to reach this frequency, but the surrounding modes should be analyzed to ensure that no modal overlap will occur at the frequency of interest.
2. Design the cavity with a coupling probe located near a position of maximum electric field at the desired mode of operation according to the field distributions in (38). Using experimentation or simulation, set the probe depth to achieve the desired level of cavity coupling. Values of $\mathscr{k}$ less than 1 are preferred, as the effects of external loading will be minimized. Avoid extremely small values of $\mathscr{k}$, though, because shallow resonances have lower signal-to-noise ratios and measurements may be inaccurate.
3. Seal the edges of the PCB laminate in a conductive material. PCB edge plating, conductive tape, or silver epoxy are all valid methods. Ensure that the plating is as smooth as possible and that good electrical contact is made between the edge conductor and both top and bottom planes.
4. Measure S_{11} of the cavity with a calibrated VNA over the frequency range of interest using a low IF bandwidth and a high number of points to maximize frequency resolution.
5. Analyze the cross section of the cavity's conductive surfaces using a microscope to determine the roughness parameters needed for the Hall Hemispherical model. If not suitable microscope is available, obtain the h_{RMS} roughness height parameter from the dielectric manufacturer. Calculate ξ using either (99) or (106), depending on the chosen roughness model.
6. Determine if the resonance is overcoupled or undercoupled by analyzing the Smith chart response.
7. Determine $\mathscr{k}$ by (112) and measuring VSWR at the resonant frequencies.
8. Calculate Q_{int} by measuring the resonance bandwidth at a suitable value of ρ and applying (121).
9. Identify the mode numbers of each resonance of interest. This can be done by finding the nearest ideal resonant frequency and its corresponding mode. The

ideal resonance frequencies should be calculated using the nominal permittivity of the material. If the nominal permittivity is not known, then the value of ϵ' must be determined by measuring the lowest frequency resonance, which is the fundamental TE_{101} mode. After the permittivity at the fundamental mode is calculated, this value may be used to then determine the mode numbers of the other resonances.

10. Solve the following equations simultaneously to determine ϵ' and $\tan(\delta_d)$. Note that the $\left(1 - \frac{1}{2Q_{smooth}}\right)$ and $\sqrt{\frac{1}{2}\left(\sqrt{1+\tan^2(\delta_d)}+1\right)}$ terms in (126) may be neglected for low loss dielectrics and highly conductive cavities. Neglecting these terms eliminates the need for simultaneous solution, and the equations may instead be solved sequentially.

$$\epsilon_d' = \left[\frac{\left(1 - \frac{1}{2Q_{smooth}}\right)\sqrt{\left(\frac{m\pi}{a}\right)^2 + \left(\frac{n\pi}{b}\right)^2 + \left(\frac{\ell\pi}{d}\right)^2}}{2\pi f\sqrt{\frac{1}{2}\left(\sqrt{1+\tan^2(\delta_d)}+1\right)}}\right]^2 \tag{126}$$

$$Q_{smooth} = \frac{4\pi f^3 \epsilon_d' \mu_d^2 a^3 b d^3}{R_s(\ell^2 a^3 d + m^2 a d^3 + 2\ell^2 a^3 b + 2m^2 b d^3)} \tag{127}$$

$$\tan(\delta_d) = \frac{1}{F(\rho,\, k)Q_\rho} - \frac{\xi}{Q_{smooth}} \tag{128}$$

4. VERIFICATION OF THE IMPROVED MODEL THROUGH NUMERICAL SIMULATION

4.1. EFFECT OF DIELECTRIC LOSS ON RESONANT FREQUENCY

To verify the very small frequency shifts predicted by (57), high simulation accuracy is required. The HFSS eigenmode solver was chosen for this task. The eigenmode solver uses a source-free method that analyzes a structure for resonance modes and returns their frequencies and Q-factors. The source-free nature of the solver eliminates any loss due to a coupling mechanism, and perfectly electrically conductive (PEC) cavity walls ensure that no power is lost in the cavity conductors. The combination of these features leads to a highly accurate resonance simulation in which the only source of loss is the dielectric material filling the cavity.

The dissipation factor of the dielectric material used in the eigenmode simulation was swept over a range of 0 to 0.05. The plot in Figure 4.1 shows the resonant frequency shift calculated by HFSS overlaid with the analytical results from Figure 3.1. The difference between analytical and HFSS calculations is shown in Figure 4.2. The match between eigenmode and analytical curves confirms that the expression for frequency in (57) is accurate and that the frequency shift due to dielectric loss is negligible for the characterization of practical materials.

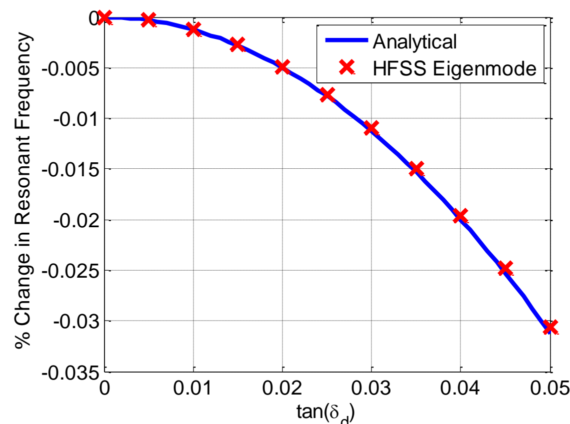

Figure 4.1. Comparison between the analytical solution and HFSS eigenmode solution of the change in resonant frequency due to dielectric loss

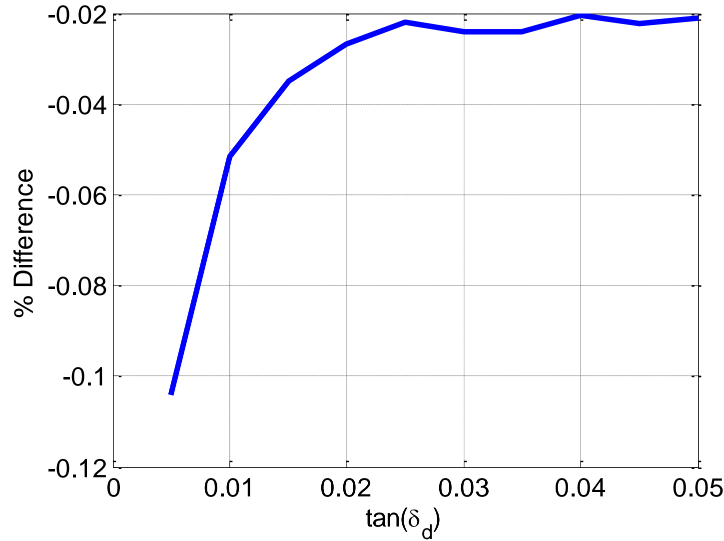

Figure 4.2. Difference between the analytical solution and HFSS eigenmode solution of the change in resonant frequency due to dielectric loss

4.2. EFFECT OF SURFACE CONDUCTIVITY ON Q-FACTOR

To determine the accuracy of the expression for Q_{smooth} given in (65), the HFSS eigenmode solver was used once again to simulate a 50x40x1 mm vacuum-filled cavity. The eigenmode solver calculates Q_{smooth} by numerically integrating the surface currents over each wall using (59). This is the same technique used in Section 3.2.1; unlike the analytical method, however, HFSS integrates the fields calculated by the eigenmode solver rather than the ideal fields that the perturbation method assumes. The use of real field distributions increases the accuracy of the calculated power loss.

A comparison of calculated Q_{smooth} between the expression in (65) and the HFSS eigenmode solver is plotted against surface conductivity in Figure 4.3. Copper, the most common PCB conductor material, has a conductivity of $\sigma_c = 5.8 \times 10^7 \frac{S}{m}$. A wider range of conductivity values is presented to verify that the analytical expression for Q_{smooth} is accurate for all practical cavity materials. Figure 4.3 indicates that Q_c increases with increasing surface conductivity. This should be expected, as higher conductivity materials exhibit lower ohmic loss. The difference between the analytical

and eigenmode curves is plotted in Figure 4.4. At $\sigma_c = 5.8 \times 10^7 \frac{S}{m}$, the analytical solutions agrees with HFSS within 0.05%, which is an acceptable level of accuracy. Figure 4.4 shows that the error between analytical and numerical solutions of Q_c decreases with increasing surface conductivity. This decreasing error is an effect of the assumption of ideal cavity field distributions. A cavity filled with a lossless dielectric will have the field distributions of an ideal cavity if its walls are perfectly conducting. As wall conductivity is decreased, the internal fields will begin to penetrate the walls (due to finite skin depth) and the field patterns will start to deviate from the ideal. This deviation from the ideal will increase with decreased conductivity, leading to the larger error in Q_{smooth} seen at lower σ_c values in Figure 4.4.

In addition to numerically simulating Q_{smooth} as a function of σ_c, eigenmode simulations were also performed at the first 15 resonant modes of the example copper-walled 50x40x1 mm cavity. The difference between these simulation results and corresponding analytical values of Q_{smooth} is shown in Figure 4.5. The highest error seen in this plot is 0.051% and occurs at the lowest resonant frequency. This error is considered acceptable.

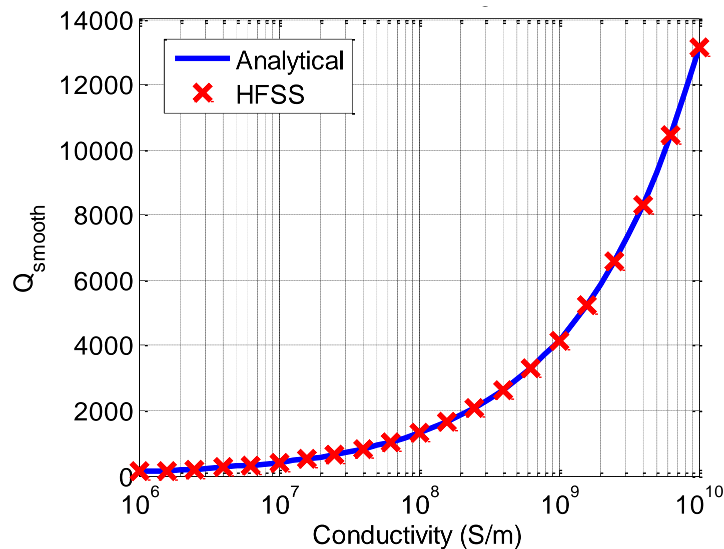

Figure 4.3. Comparison between the analytical solution and HFSS eigenmode solution of Q_{smooth} as a function of cavity wall conductivity

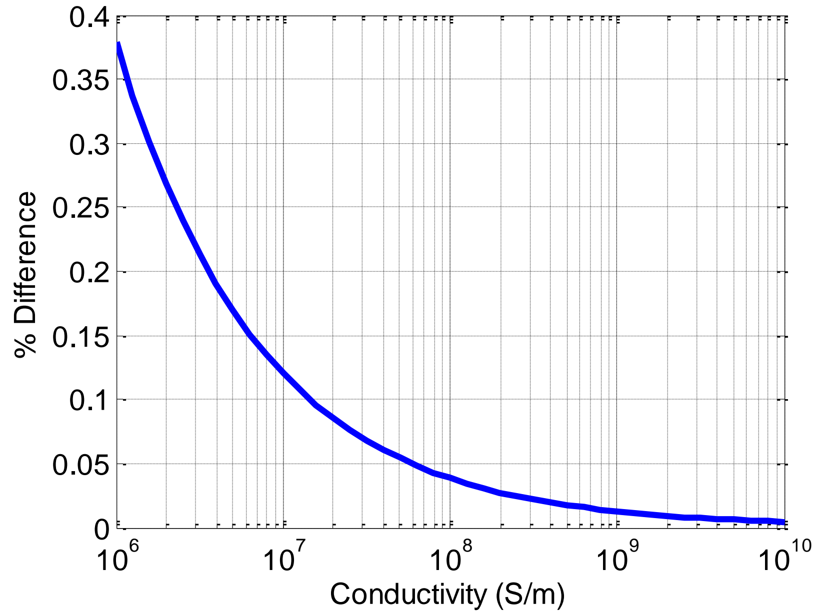

Figure 4.4. Difference between the analytical and HFSS eigenmode solutions of Q_{smooth} as a function of surface conductivity

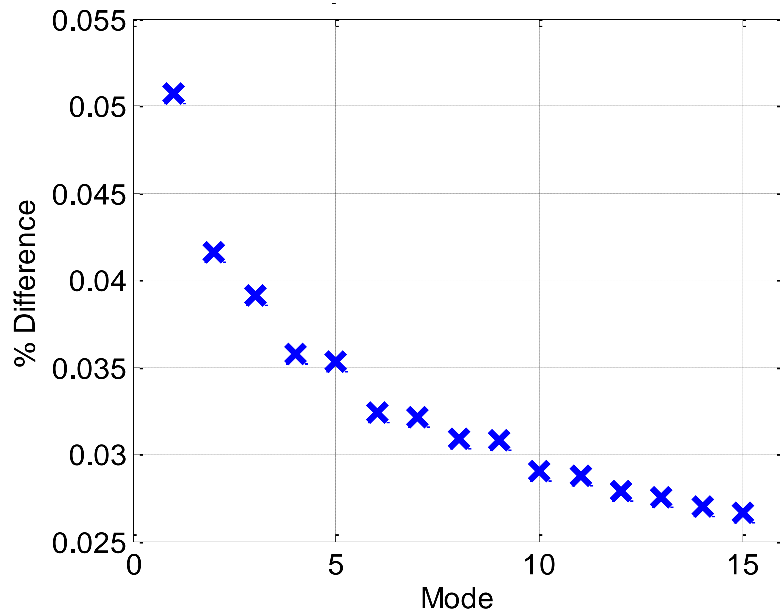

Figure 4.5. Difference between the analytical and HFSS eigenmode solutions of Q_{smooth} as a function of resonant mode for an example cavity

4.3. EFFECT OF SURFACE CONDUCTIVITY ON FREQUENCY

The HFSS eigenmode solver was used to calculate the resonant frequency of a vacuum-filled 50x40x1 mm cavity operating in the TE_{101} mode with varying values of wall conductivity. The eigenmode results are overlaid with the analytical results calculated by (65) and (96) in Figure 4.6. The difference between the simulated and analytical values of f_r as a function of σ_c is shown in Figure 4.7. For copper, the difference was found to be less than 0.01 PPM.

To ensure that the calculated shift in f_r is valid over multiple modes, the difference between simulated and analytical resonant frequencies for the first 15 modes of a copper-clad cavity was calculated and plotted in Figure 4.8. The difference does not exceed 1 PPM. The strong agreement between the eigenmode and analytical solutions confirms the validity of (96).

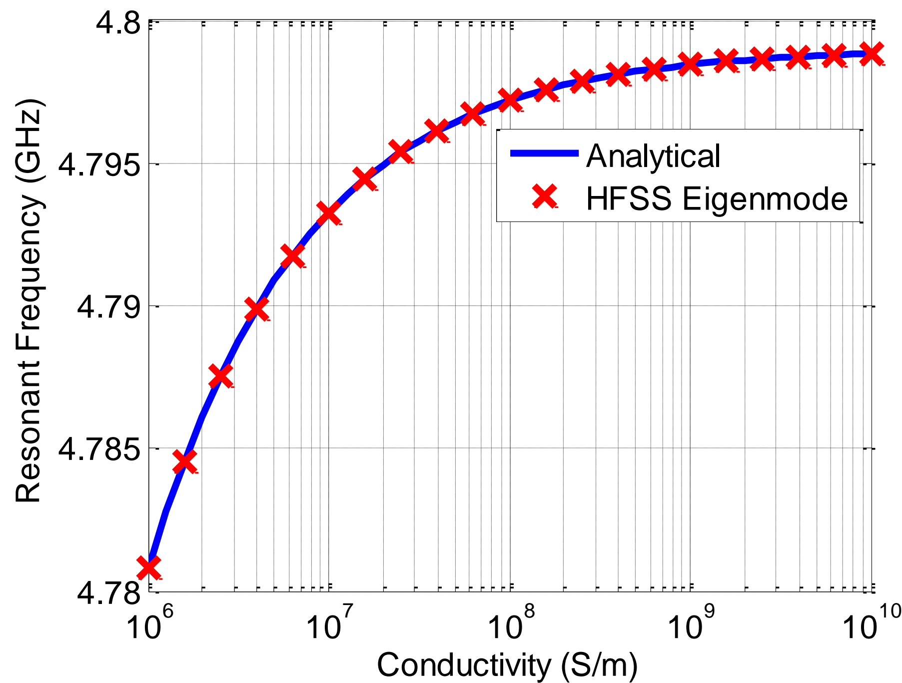

Figure 4.6. Comparison between the analytical and HFSS eigenmode solutions of f_r as a function of σ_c for an example cavity

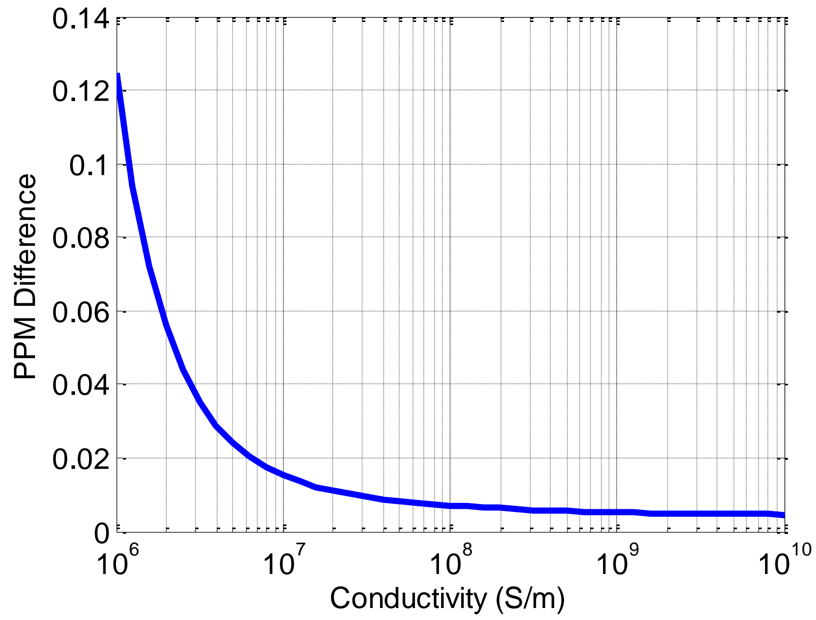

Figure 4.7. Difference between the analytical and HFSS eigenmode solutions of f_r as a function of σ_c for an example cavity

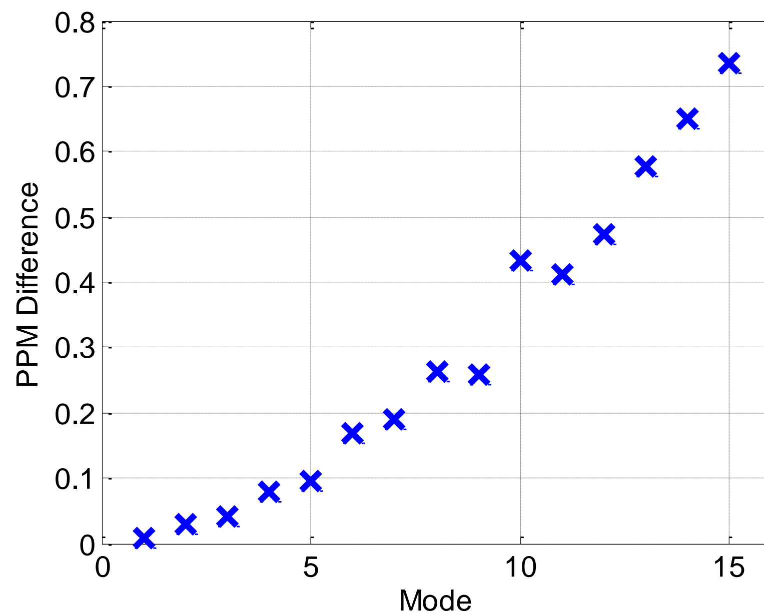

Figure 4.8. Difference between the analytical and HFSS eigenmode solutions of f_r as a function of resonant mode for an example cavity

4.4. EFFECT OF CONDUCTOR SURFACE ROUGHNESS ON Q-FACTOR

Due to the small feature size of a rough conductor surface, any full wave simulations involving surface roughness require an extremely fine mesh. The number of mesh cells needed to simulate a large surface area lead to prohibitively high memory and CPU requirements. It therefore becomes necessary to simplify the simulation model so that it may be run with modest computing resources.

To begin simulated analysis of the effects of surface roughness, a 1 mm long stripline model was constructed in CST. An image of the stripline structure is shown in Figure 4.9. $|S_{21}|$ was simulated over the 1-15 GHz frequency range for both smooth and rough stripline surface textures. The rough surface was created on one side of the stripline by using MATLAB to build a series of hemispheres in CST through the VBA interface. 2500 hemispheres were created over the stripline with a uniformly random distribution, as shown in Figure 4.10. The radii of the spheres followed a Gaussian distribution. The resulting positions and radii of the hemispheres were used to calculate the three surface parameters needed by the Hall Hemispherical model. These parameters are listed in Table 4.1. The value of ξ over frequency for these surface parameters is shown in Figure 4.11.

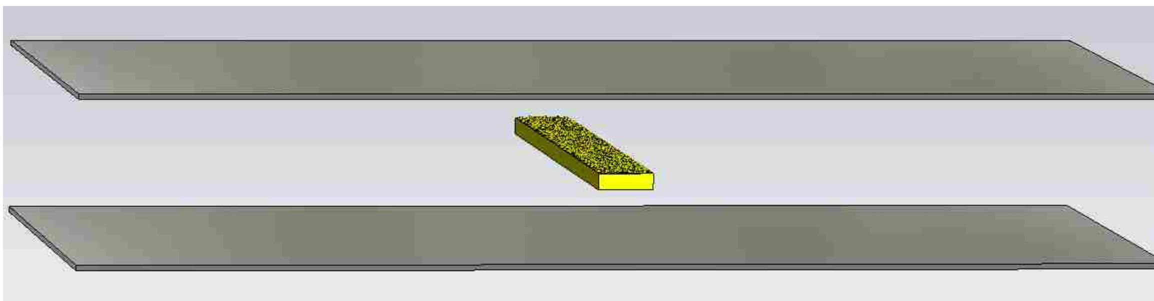

Figure 4.9. Simulated stripline structure used to model the effects of conductor surface roughness

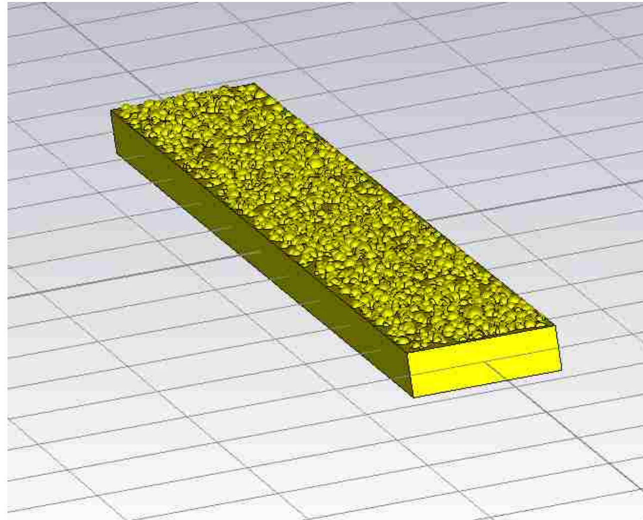

Figure 4.10. Close-up image of the rough stripline model used in simulation

It is important to note that the surface profile simulated in CST is not entirely realistic. It is extremely difficult to accurately model the complexities of a real rough conductor surface without being able to import data from a profilometry scan, which was not feasible for this study. Because the simulated surface profile matched closely with that assumed by the Hall model, this simulation was not intended to rigorously analyze the validity of the aforementioned model. Rather, these simulations sought to determine the level of agreement between full wave simulation and a model that has been proven accurate through experimental tests. In this way, the stripline simulation served as a loose validation technique for the accuracy of the CST roughness model and associated mesh settings.

The time-domain finite integration technique (FIT) solver in CST was chosen over a frequency domain FEM solver because of the lower memory consumption of the time domain algorithm and the availability of a high performance computing cluster that was only capable of running the FIT algorithm. A hexahedral mesh was used, and the surface roughness was meshed with a resolution of $0.5\ \mu m$. Increasing the mesh resolution was found to make very little difference in the simulated results, thus

confirming the validity of the 0.5 μm mesh. The resulting simulation consisted of roughly 100 million mesh cells and took nearly 24 hours to complete.

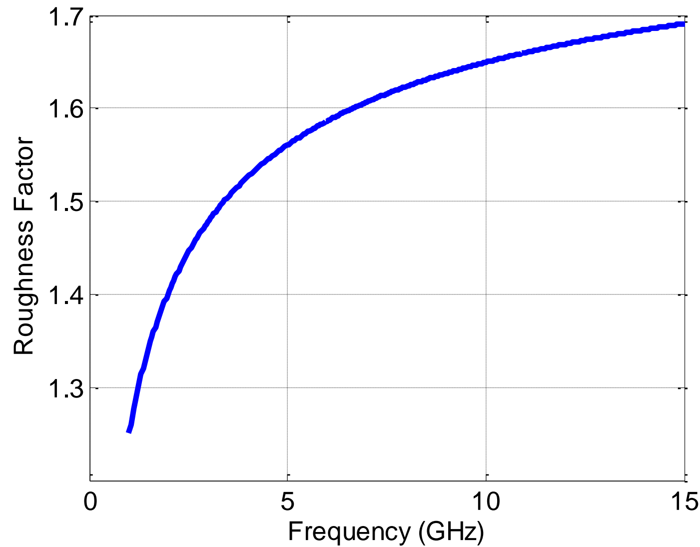

Figure 4.11. Calculated roughness factor for simulated stripline surface

Simulated $|S_{21}|$ results are shown in Figure 4.12. The Hall model was found to match very closely with the FIT results. Because of this agreement, simulations of a cavity with a rough top surface were attempted. It soon became apparent that the computational resources required for modelling surface roughness on the top plane of a cavity exceeded that of the available computers.

Another cavity model was created, this time with only a single side wall being roughened. The memory requirements were still too great for an FEM solver to be used, so the FIT algorithm was used once again. Time domain solvers are typically a poor choice for use in simulating resonant structures because of the amount of simulation time required for the energy in the excitation signal to decay. Nevertheless, FIT was the only solver capable of running the simulation. After several attempts to get usable data from

the FIT cavity simulations, the results were never considered accurate enough for any kind of analysis. Resonant frequencies and Q-factors of cavities with smooth walls were never in agreement with the results from FEM simulations of the same model. As such, it was decided that cavity roughness would have to be analyzed through measurement rather than numerical simulation, and no further surface roughness simulations were performed.

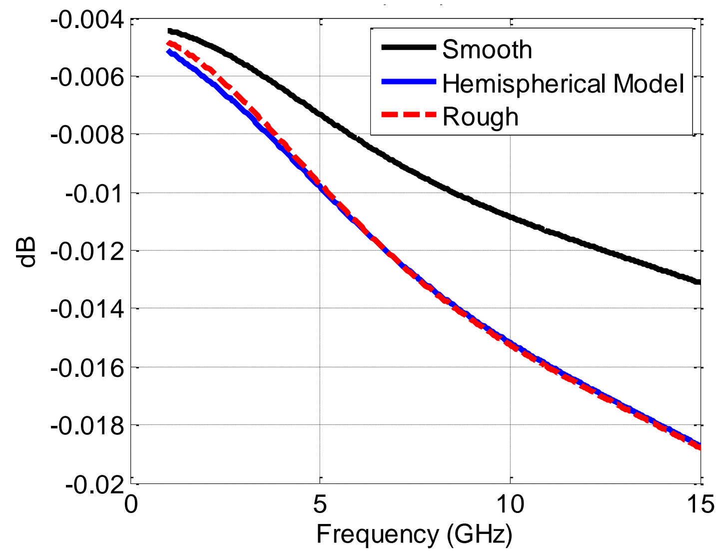

Figure 4.12. Comparison of simulated $|S_{21}|$ results of a rough stripline and the Hall Hemispherical model

Table 4.1. Simulated surface roughness parameters

h_{RMS}	$3\ \mu m$
B_{RMS}	$6\ \mu m$
s_{RMS}	$10\ \mu m$

4.5. EFFECT OF CAVITY COUPLING ON Q-FACTOR

To verify the accuracy of the Q_{int} values calculated in Section 3.5.2, the HFSS eigenmode solver was used to determine the Q-factor of the cavity without the effect of external loading. The analytically calculated values of Q_{int} were compared to the HFSS solution at each value of $\mathscr{k}$, and the resulting difference is shown in Figure 4.13. For small values of $\mathscr{k}$, the difference is under 0.5%. The difference is greater for overcoupled cavities (i.e., $\mathscr{k} > 1$). This greater difference is likely due to the assumption made in (117), which begins to lose validity at low values of Q.

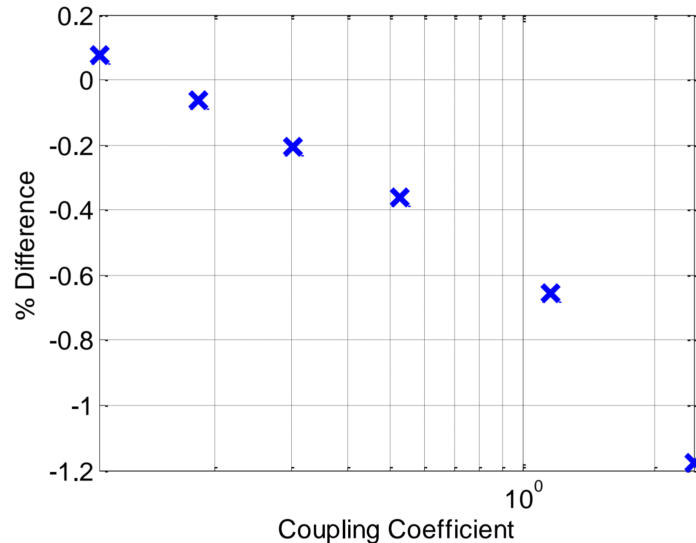

Figure 4.13. Difference between analytical and HFSS eigenmode solutions of Q_{int} as a function of $\mathscr{k}$

4.6. SIMULATED DIELECTRIC CHARACTERIZATION

The dielectric characterization procedure outlined in Section 3.7 was performed on a simulated cavity to provide validation of the procedure. Because of the difficulties in simulating surface roughness, smooth cavity walls were used in the simulation and it

was assumed that $\zeta = 1$. All other non-ideal effects addressed in this thesis were considered.

The cavity model used in Section 3.5.2 was repurposed for use in the simulated dielectric characterization. The walls were composed of copper and the interior of the cavity was filled with Rogers 4350. Dielectric dispersion was disabled in the simulation to ensure that ϵ' and $\tan(\delta)$ did not change with frequency. A probe depth of 0.6 mm was used.

The $|S_{11}|$ results of a frequency sweep from 1 GHz to 10 GHz are shown in Figure 4.14. This figure indicates that there are five usable modes in the frequency span. Modal overlap occurs near 10 GHz, making that resonance unusable.

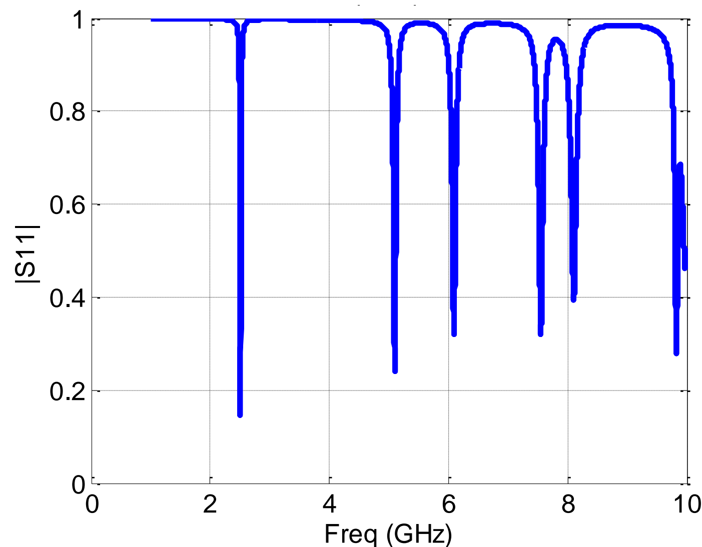

Figure 4.14. Simulated $|S_{11}|$ used to test dielectric characterization procedure

The results from the dielectric characterization procedure for each of the five usable modes are shown in Table 4.2. The extracted values of $\tan(\delta_d)$ do not vary more than 5% (+2 counts) from the ideal value of 0.004. The extracted values of ϵ_r' do not vary more than 0.8% ($+2$ counts, -3 counts) from the simulated permittivity of 3.66.

The error in ϵ_r' is caused by the loading effect of the cavity feed on the resonant frequency, which is not considered in this model. The error in $\tan(\delta_d)$ appears to increase with frequency, which may be attributed to the fact that $\hbar$ was observed to also increase with frequency. Figure 4.13 illustrates that error in measured Q_L and $\tan(\delta_d)$ increases with $\hbar$, so a small frequency dependence of error is not unexpected. Table 4.2 also lists the uncorrected values of $\tan(\delta_d)$ for which none of the non-ideal effects were considered. The uncorrected dissipation factors exhibit error ranging from 200%-380%. This large error clearly shows the importance of including non-ideal effects in the improved planar cavity model.

Though small errors are present in the characterization of the simulated dielectric material, the results overall are promising. The dielectric characterization procedure is validated for cavities with smooth walls. Physical measurements are required to validate the model in the presence of surface roughness.

Table 4.2. Simulated dielectric characterization results

Frequency (GHz)	$\boldsymbol{\epsilon_r'}$ **(Spec: 3.66)**	$\boldsymbol{\tan(\delta_d)}$ **(Spec: 0.0040)**	**Uncorrected** $\boldsymbol{\tan(\delta_d)}$
2.5	3.65	0.0040	0.0123
5.1	3.65	0.0041	0.0168
6.1	3.68	0.0040	0.0179
7.5	3.63	0.0041	0.0180
8.1	3.64	0.0042	0.0191

5. VERIFICATION OF THE IMPROVED MODEL THROUGH PHYSICAL MEASUREMENT

5.1. CAVITY CONSTRUCTION

Two cavities were constructed out of 62 mil thick Rogers 5880 sheets. One cavity measured 55.3x50.0x1.57 mm while the other cavity measured 58.3x49.8x1.57 mm. The former is shown in Figure 5.1. The edges of both cavities were cut as straight and parallel as possible using a mill. The size of the cavities was determined by the geometry of the mill's clamp table. A through-hole SMA connector was used as the coupling probe on each cavity. The connectors had four GND pins at the corners that had to milled off, as shown in Figure 5.2. The center pin was cut to an approximate length of 0.7 mm by hand, as it was too fragile to be milled. A flat-bottomed 3/16" hole was drilled in the top copper plane to provide access to the inner dielectric. A 3/32" hole was then drilled 50% through the dielectric to provide room for the SMA center pin. The SMA pin was aligned with the dielectric hole and the brass shell of the SMA connector was soldered onto the copper plane with 360° coverage.

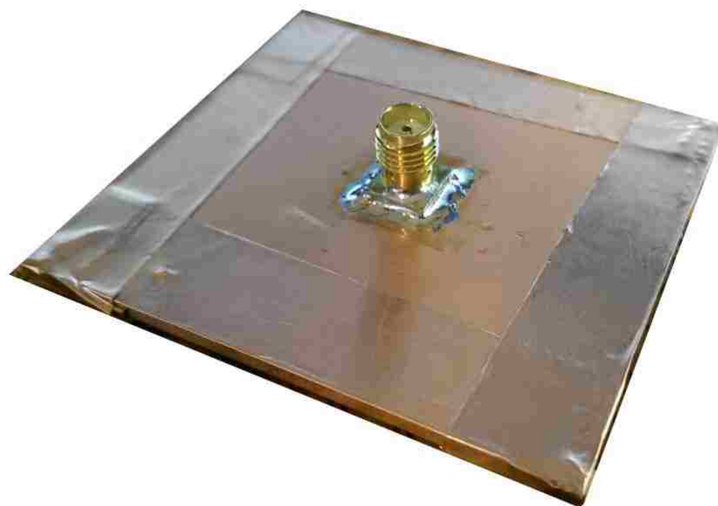

Figure 5.1. 55x50x1.6 mm cavity made with Rogers 5880 laminate

Figure 5.2. Milling process for removing SMA GND pins

Copper tape was used to seal the edges of the cavity. Care was taken to ensure that the tape was as flat and smooth as possible, and that adequate pressure was used to ensure a good electrical connection between the tape and the copper planes.

5.2. SURFACE ROUGHNESS MEASUREMENTS

A section of laminate material was cut off the panel for SEM cross sectional imaging. The edge was polished and imaged in several locations. Images of the surface roughness are shown in Figure 5.3 and Figure 5.4. The roughness profile was manually characterized by analyzing a series of images similar to Figure 5.4. The measured parameters are listed in Table 5.1 and the resulting roughness coefficient ξ is plotted against frequency in Figure 5.5. The measured inclusion height parameter h_{RMS} was found to be larger than that specified by the manufacturer. It is possible that this discrepancy is attributable to manual measurement error, but the value was confirmed by repeated measurement. The measured and specified values are near enough to each other that the difference could be within the non-published tolerance of the material.

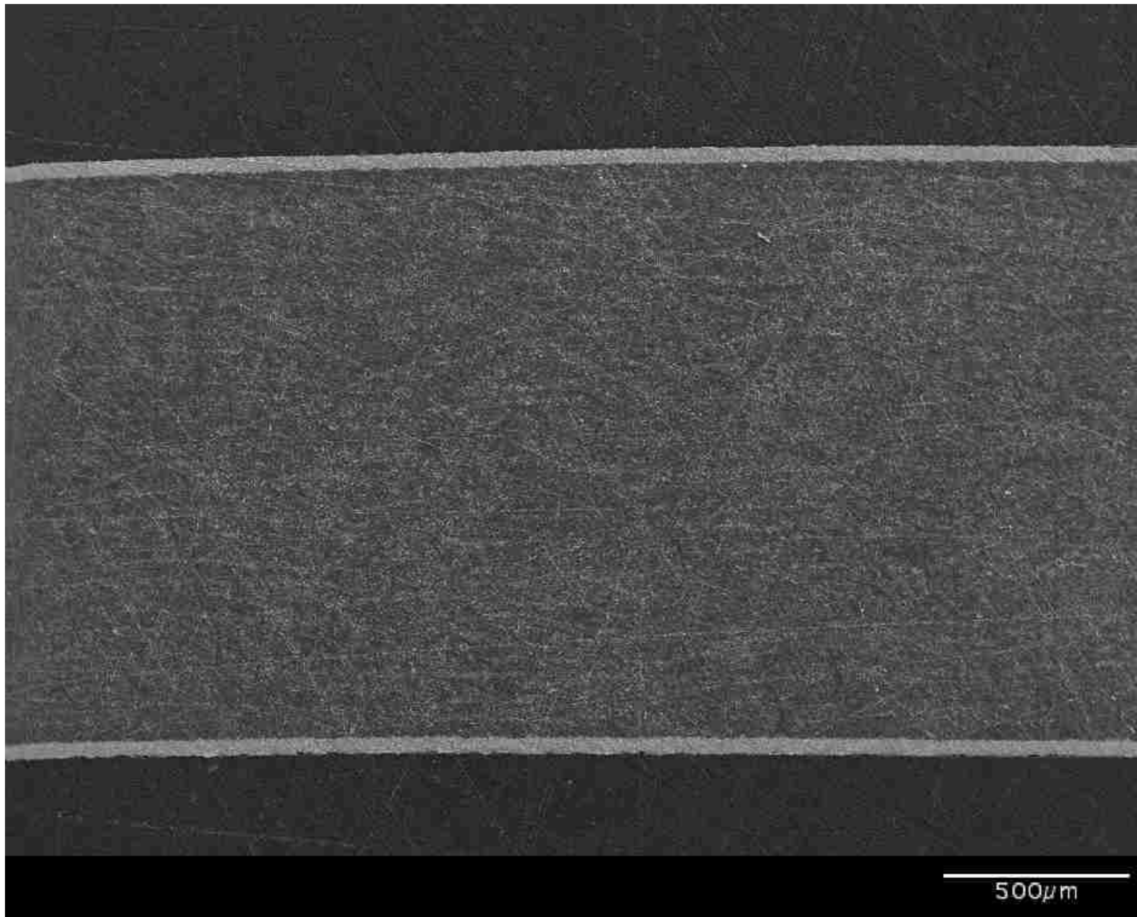

Figure 5.3. SEM image of PCB laminate cross section

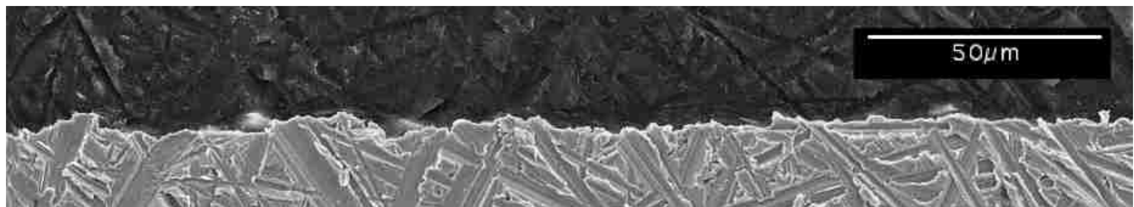

Figure 5.4. SEM image of conductor surface roughness

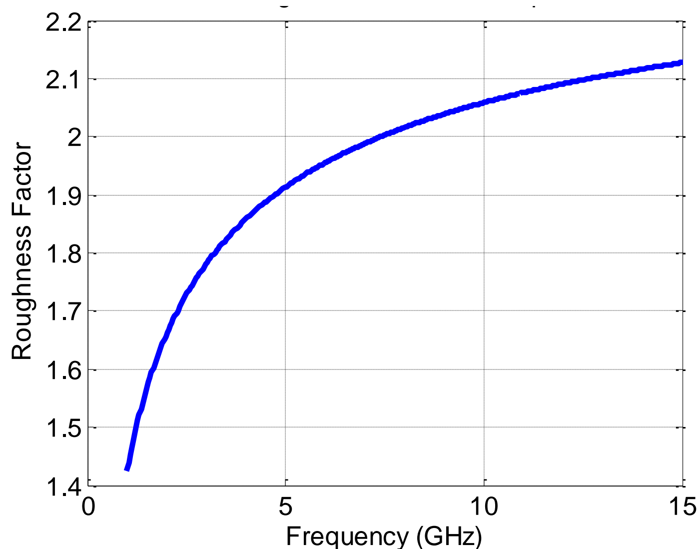

Figure 5.5. Calculated roughness coefficient vs. frequency for physical cavity

Table 5.1. Measured roughness parameters

h_{RMS}	3.0 μm (Spec: 2.1 μm)
B_{RMS}	7.6 μm
s_{RMS}	7.0 μm

5.3. ELECTRICAL MEASUREMENTS

A 20 GHz VNA was used to perform reflection measurements on the two laminate cavities. To ensure high resolution in both amplitude and frequency, 12001 points were measured with an IF bandwidth of 500 Hz. SOL calibration was performed at the end of the VNA's cable, and a port extension of 42 psec was used to extend the reference plane to the cavity wall. Figure 5.6 shows the measured reflection of the 55.3x50 mm cavity on a linear scale. There are clearly five strong resonances with which dielectric properties can be measured. From the Smith chart representation in Figure 5.7, it was determined that all resonances were undercoupled. Results from the

58.3x49.8x1.57 mm were visually similar, though resonances occurred at slightly different frequencies due to the size differences.

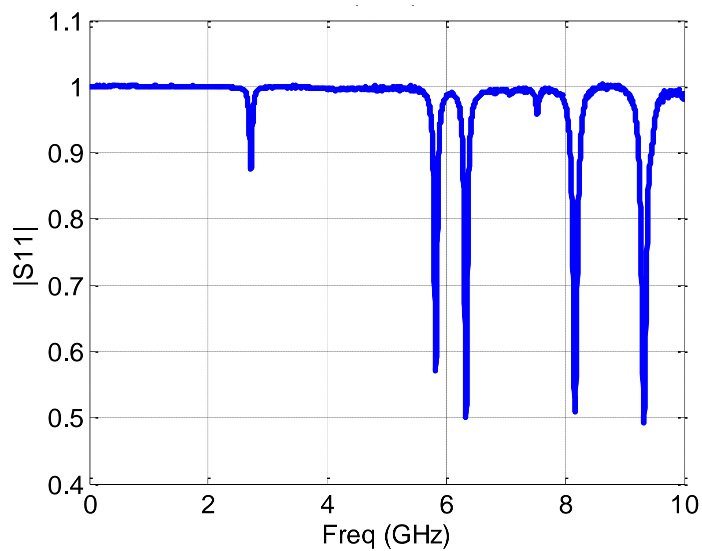

Figure 5.6. Measured reflection response of 55.3x50.0x1.57 mm cavity

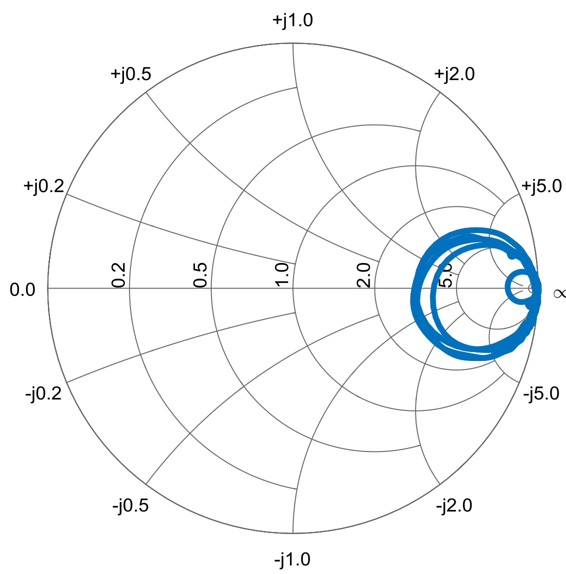

Figure 5.7. Smith chart representation of measured reflection response

The procedure in Section 3.7 was used to determine the dielectric properties at each resonant frequency. The results for both cavities are listed in Table 5.2 and Table 5.3.

Table 5.2. Measured dielectric properties for 58.3x49.8 mm cavity

Freq. (GHz)	ϵ_r' **(Spec: 2.2** ± 0.02**)**	$\tan(\delta_d)$ **(Spec: 0.0004 @ 1 MHz 0.0009 @ 10 GHz)**	**Uncorrected** $\tan(\delta_d)$
2.70	2.150	0.00008	0.0009
5.58	2.203	0.0005	0.0017
6.32	2.208	0.0008	0.0018
7.99	2.203	0.0014	0.0023
8.90	2.202	0.0010	0.0019

Table 5.3. Measured dielectric properties for 55.3x50.0 mm cavity

Freq. (GHz)	ϵ_r' **(Spec: 2.2** ± 0.02**)**	$\tan(\delta_d)$ **(Spec: 0.0004 @ 1 MHz 0.0009 @ 10 GHz)**	**Uncorrected** $\tan(\delta_d)$
2.72	2.210	0.00048	0.0013
5.82	2.215	0.0015	0.0027
6.32	2.207	0.0017	0.0028
8.16	2.205	0.0024	0.0034
9.31	2.220	0.0029	0.0040

5.4. ANALYSIS

It is difficult to calculate an absolute value of accuracy for the measured data in Table 5.2 and Table 5.3 because the exact values of ϵ_r' and $\tan(\delta_d)$ of the material are

unknown. Nevertheless, the manufacturer specifies a tolerance of ± 0.02 (1%), and all but one of the measured permittivity values falls within this range. The negligence of the detuning caused by reactive coupling may explain the deviation in ϵ_r' between the two cavities. An error of similar magnitude was seen in the simulated characterization procedure in Section 3.7, where the coupling detuning was also thought to be responsible for the variations in calculated ϵ_r'.

The dissipation factor is specified by the manufacturer as 0.0009 at 10 GHz. It is expected, then, that the measured $\tan(\delta_d)$ would increase throughout the measured frequency range and approach 0.0009 at the highest measured frequency. While the measured loss is indeed seen to increase with frequency (excluding a single exception between 7.99 GHz and 8.90 GHz in the 58.3x49.8 mm cavity), both sets of measurements indicate a higher final value of loss than the manufacturer's specification. It is important to note that the It seems likely that the surface roughness characterization is at least a partial culprit, since the surface profile measurements were made on only a small cross section of the total material. An inadequate roughness characterization could partially explain the error seen at lower frequencies, but, as explained in Section 3.4.4, the error due to inaccurate surface profiling will tend to decrease at higher frequencies.

An additional source of loss is the surface conductivity of the copper tape used to form the cavity walls. The tape was assumed to have the conductivity of pure copper, though in reality the conductive adhesive that forms the innermost surface of the cavity walls is less conductive than the pure metal. The relatively low contribution of power lost in the side walls to overall Q-factor suggests that the error due to the adhesive's conductivity is not sufficiently large to explain the discrepancies seen, especially in the 55.3x50 mm cavity.

Of greater interest than the measured increase in loss at high frequencies is the fact that two cavities have dissipations factors that differ by over 100% near 9 GHz. A difference in conductor roughness profile between the two cavities may have existed. The laminate sample that was imaged with the SEM was taken from a region on the panel that was physically closer to the 58.3x49.8 mm cavity than the 55.3x50.0 mm cavity. It is unlikely, though, that surface roughness would vary sufficiently over the surface of a panel to create the differences seen in the measured results.

The difference in measured $\tan(\delta_d)$ seen between the two cavities suggests the possibility that another loss term may exist that has not yet been identified. Both cavities were of similar physical size and were constructed of the same materials using the same techniques. The cavity feed was the least controlled element of the system and seems to be a probable location for additional loss. Attempts to reproduce the additional loss were made in simulation by introducing probe tilt and liftoff between the SMA shell and the cavity body. Tilting the probe by 10 degrees was found to provide no additional loss that was not compensated by the feed de-embedding equation in (121). A 0.5 mm air gap was found to introduce some additional loss, but not enough to account for the 100% error found in the measurements.

Radiation loss was assumed to be negligible due to the totally enclosed nature of the cavity. It is possible, however, that poor adhesive conductivity of the copper tape allowed power to be radiated from the seams along the cavity edges. Further study is necessary to identify the presence of unwanted radiation.

6. CONCLUSION

The research presented in this thesis attempted to develop an improved planar cavity model that de-embeds the cavity's non-ideal effects from resonance measurements to enable accurate calculations of dielectric permittivity and dissipation factor. The effects on resonant frequency that were analyzed included dielectric loss and cavity wall reactance. The effects on quality-factor included cavity wall resistance and surface roughness, as well as external loading caused by the coupling network. Each of these non-ideal effects was mathematically modelled and verified through numerical simulation.

One known source of error in resonant frequency was not able to be modelled—the effect of external coupling reactance. A published empirical technique for calculating this effect was tested, but the results fundamentally did not agree with numerous simulations. Additional research should be performed to better account for this non-ideal behavior.

Measurement of two physical cavities was performed, and the dielectric characterization method developed in this thesis was used to extract the cavity's substrate properties. The results were promising, though not consistent enough to be fully trusted. A discrepancy existed between the calculated dissipation factors of the two cavities that suggests the possible existence of a fourth quality factor error term. Additional cavities should be constructed to investigate this possibility.

Despite the failure to model the coupling network's effect on resonant frequency or to achieve highly consistent measurement results, the research performed in this thesis provides a strong foundation for future work into improving the accuracy of the planar cavity model.

BIBLIOGRAPHY

[1] A. Sihvola, *Electromagnetic Mixing Formulas and Applications*, IET, 2008.

[2] C. A. Balanis, *Advanced Engineering Electromagnetics, 2nd Edition*, Wiley, 2012.

[3] Keysight Technologies, "Basics of measuring the dielectric properties of materials".

[4] Institute for Interconnecting and Packaging Electronic Circuits, "IPC-TM-650 Test Methods Manual," 1989.

[5] D. M. Pozar, *Microwave Engineering, 4th Edition*, Wiley, 2012.

[6] Rogers Corporation, "RO4000 Series High Frequency Circuit Materials Data Sheet," 2015.

[7] A. E. Karbowiak, "Theory of imperfect waveguides: The effect of wall impedance," *Proceedings of the IEE - Part B: Radio and Electronic Engineering,* vol. 102, no. 5, pp. 698-708, 1955.

[8] J. J. Gustincic, "A general power loss method for attenuation of cavities and waveguides," *IEEE Transactions on Microwave Theory and Techniques,* vol. 11, no. 1, pp. 83-87, 1963.

[9] O. Jensen and E. Hammerstand, "Accurate models for microstrip computer-aided design," *IEEE MTT-S Digest,* pp. 407-409, 1980.

[10] G. Brist, S. Clouser and T. Liang, "Non-classical conductor losses due to copper foil roughness and treatment," *ECW 10 Conf. at IPC Circuits Designers Summit,* pp. S19-2-1-S19-2-1-11, 2005.

[11] Rogers Corporation, "Copper foils for high frequency materials," 2015.

[12] P. Huray et. al, "Impact of copper surface texture on loss: A model that works," *DesignCon 2010,* vol. 1, pp. 462-483, 2010.

[13] Stephen Hall et. al., "Multigigahertz causal transmission line modeling methodology using a 3-D hemispherical surface roughness approach," *IEEE Transactions on Microwave Theory and Techniques,* vol. 55, no. 12, pp. 2614-2624, 2007.

[14] S. Morgan, "Effect of surface roughness on eddy current losses at microwave frequencies," *Journal of Applied Physics,* vol. 20, pp. 352-362, 1949.

[15] R. S. Kwok and J.-F. Liang, "Characterization of High-Q Resonators for Microwave Filter Applications," *IEEE Transactions on Microwave Theory and Techniques,* vol. 47, no. 1, pp. 111-114, 1999.

[16] A. J. Canós et. al., "A new empirical method for extracting unloaded resonant frequencies from microwave resonant cavities," *IEEE MTT-S International Microwave Symposium Digest,* pp. 1823-1825, 2003.

VITA

Benjamin Conley was born on November 17, 1990 in St. Louis Missouri. He completed his Bachelor's of Science degree in Electrical Engineering from the Missouri University of Science and Technology in May 2014. Ben began working as a graduate research assistant with the Electromagnetic Compatibility Laboratory at MS&T that same month. In December 2015, he received his Master's Degree in Electrical Engineering from the Missouri University of Science and Technology.